International Information and Engineering Technology Association
Advancing the World of Information and Engineering

International Journal of Heat and Technology
Vol. 43, No. 2, April, 2025, pp. 583-602
Journal homepage: http://iieta.org/journals/ijht

Heat and Mass Transfer in Magneto-Dissipative Buongiorno Nanofluid Flow Along a Semi-Infinite Plate in a Non-Darcy Porous Medium

Asra Anjum[1,2*], Deevi Sateesh Kumar[1], Shaik Abdul Gaffar[2], Samdani Peerusab[3]

[1] Department of Engineering Mathematics, Koneru Lakshmaiah Education Foundation, Guntur 522302, India
[2] Mathematics and Computing Skills Unit, Preparatory Studies Centre, University of Technology and Applied Sciences, Salalah 211, Sultanate of Oman
[3] Department of Engineering, University of Technology and Applied Sciences Salalah 211, Sultanate of Oman

Corresponding Author Email: asraanjum84@gmail.com

https://doi.org/10.18280/ijht.430220

Received: 10 February 2025
Revised: 8 April 2025
Accepted: 22 April 2025
Available online: 30 April 2025

Keywords:
Nanofluid, semi-infinite vertical plate, viscous dissipation, magnetic parameter, skin friction, Brownian motion, thermophoresis, finite difference technique

ABSTRACT

A comprehensive theoretical and computational investigation is carried out on nonlinear, steady-state, laminar convective boundary layer flows of an incompressible Buongiorno-type nanofluid from a semi-infinite vertical surface embedded within a non-Darcy porous medium. The Darcy-Forchheimer model is deployed for the porous medium. “The research investigation fills a major vacuum in the literature by integrating the above-mentioned effects with Buongiorno’s nanofluid model.” The versatile second-order accurate implicit finite-difference Keller Box technique is used to solve the dimensionless nonlinear BVP “An excellent correlation is obtained on validating the present results with the previous research results available in the literature and the error analysis is also examined.” “The novelty of the present work is the insights into the structure of nanofluids in porous media, heat and mass transfer”. It is observed that the velocity profile is enhanced with increment in (M) whereas temperature and concentration profiles are suppressed with a larger Darcy number, velocity is strongly increased near the surface, whereas temperature, concentration is depleted throughout the boundary layer with greater Darcy number. An augmentation in the Forchheimer number significantly suppresses the fluid velocity, while concurrently enhancing both the thermal and solutal profiles. This current study has practical implications in enhancing the design and optimization the cooling systems, electronic thermal management, and energy systems. This study makes major advances to the fields of thermal sciences and nanofluid technology dynamics.

1. INTRODUCTION

Nanofluid (NF) is a combination of nanostructures and a fundamental fluid. Nanofluid technology is the most efficient heat transmission method. Numerous scientists have anticipated that NFs will be able to convey heat more efficiently than basic fluids. By suspending nanoparticles (NPs) smaller than 100 nm in ethylene glycol, water, and oil, nanofluids can be altered. The heat conductivity of these fluids containing NPs suggests a substantial role as a route for thermal and mass transmission. An elevation in thermal conductivity significantly improves a fluid's ability to transmit heat. Choi [1] proposed the term "nanofluid" to address new heat transfer challenges using nanotechnology. Eastman et al. [2] also reviewed substantial research on convective transport in NFs. Buongiorno [3] developed this model in 2006, considering the impacts of two significant mechanisms namely Brownian motion and thermophoresis. These mechanisms greatly influence the properties of NFs related to heat transmission. The model more accurately depicts patterns of NFs in myriad ways. Buongiorno provided a thorough synopsis of several studies on heat transmission and thermal conductivity in NFs. Utilizing the Buongiorno nanofluid (BNF) framework, Ahmad et al. [4] conducted an in-depth investigation into the unsteady dynamics of NF thin films distributed over a rotating disk, accounting for the influences of Lorentz forces and an imposed magnetic field. Important discoveries include the lowering of film thickness with rotation and unsteadiness, as well as the enhancement of heat transfer rates through thermophoresis and Brownian motion. According to Khan et al. [5], asymptotic patterns appear for the shear-to-strain rate ratio at infinity, while viscoelasticity and magnetic fields greatly reduce displacement thicknesses. The complex interactions between fluid characteristics and outside influences on NF flow dynamics are emphasized by these effects. Multiple solutions of non-homogeneous Sisko fluid flow over stretching/shrinking sheets were examined by Ahmad et al. [6], considering suction/injection effects, magnetic fields, and varying thermal conductivity. Reduction of skin friction with material characteristics and clear patterns in temperature and concentration profiles because of relaxation parameters are important discoveries. Uddin et al. [7] computed using a Galerkin FEM, the unsteady convection flow of ferric oxide-water Buongiorno nanofluids within the annulus formed between a square and a concentric hypocycloid. They noted that a significant boost is computed in heat transfer with increment in volume fraction whereas the converse effect is produced with greater nanoparticle diameter. Humane et al. [8] investigated Buongiorno modeled Nano liquid of thermal and concentration-driven convective phenomena are explored within a magneto-micropolar fluid confined to an inclined, porous, and elastically stretching medium, highlighting the intricate interplay between heat and mass transfer under the influence of magnetic and microstructural fluid effects. Numerous engineering applications require large thermal transmissions. This has a variety of applications, including safer surgery through heat treatment, medicinal applications like cancer therapies, and solar energy applications like heat exchanger building. For practical applications, more effective oils and lubricants can be made thanks to NF technology. Thermal and solid-state stratification have several real-world uses due to NFs' mass and heat transport.

The Darcy number (*Da*) is a dimensionless measure that describes how fluids pass through porous materials like rock or soil. It is called after the French engineer Henry Darcy, who was a pioneer in the investigation of fluid dynamics in porous media. Defined as proportionate of permeability of porous media to characteristic length scale squared. The Darcy model [9] is the most well-known example of this type of model and is typically applicable to flows with high viscosity or low Reynolds numbers. In accordance with this theoretical framework, a direct linear correlation exists between the fluid velocity and the pressure gradient traversing the porous medium, implying proportional resistance to flow within the medium's structure. In fluid mechanics, the dimensionless Forchheimer number (*Fs*) is used to describe how important viscous forces are with inertial forces in a porous material. In 1901, a Dutch engineer by the name of P. Forchheimer expanded on Darcy's ideas by using it as a foundation. When computing the inertial forces in the momentum equation, Forchheimer [10] added square of the velocity term, modifying Darcy's Law. The Forchheimer number serves as a pivotal dimensionless parameter that elucidates the comparative influence of inertial forces relative to viscous forces-regulated by the fluid's dynamic viscosity—within the flow through a porous medium. Muskat [11] incorporated this expression into his work; it is now referred to be a "Forchheimer term." Later, Pal and Mondal [12] examined Darcy-Forchheimer (*Da-Fs*) model in their research, discovering that the NF concentration profile's declaration increases the electric field parameter. It is frequently applied to flow analysis through porous media, including filter media, packed beds, and porous membranes. The porosity of the medium is characterized as the ratio of the pore volume to the total volume of the medium. While there are innumerable naturally existing porous media, some are artificially created to meet industrial needs. Stones such as limestone, sandstone, fabric sponges, human skin, kidneys, gallbladders with stones, etc. are examples of naturally permeable media. One of the most diverse areas of contemporary engineering science is transport in porous mediums. Hybrid coatings designed for offshore platform structures [13] have evolved significantly. Over the past century, there has been a consistent advancement in the mathematical modelling of fluid dynamics within porous media. A thorough analysis is carried out to assess the natural thermal conduction in magnetohydrodynamic flow within a square enclosure, which undergoes differential heating and is filled with a uniform non-Darcian porous medium saturated with a HNF (TiO_2/Cu–water), Venkatadri et al. [14] demonstrated that while a larger Hartmann magnetic number and (*Fs*) significantly reduce movement, they also increase the flow of heat to the interface. Ultimately, they discovered that a low Hartmann number, low nanoparticle volumetric fraction, and high (*Da*) maximize thermal transfer rates utilizing a response surface methodology (RSM) technique. Ferdows et al. [15] conducted more research on non-Darcy convection by utilizing the MATLAB BVP4C function to examine the impact of on the combined gyrotactic bioconvection flow emanating from a horizontal cone towards a non-Darcian porous surface is examined.

Chemical engineering polymer spin coating techniques allow for the exact deposition of an external coating on a rotating topology. The use of this method for creating thin polymeric coatings has grown in recent years. Thermal conduction frequently occurs in conjunction with spin coating. To further modify the coating properties, a porous medium can be placed outside of the rotating body (substrate). This has led to a few researchers studying the convection of the BL from spinning objects in relation to non-Darcian porous materials [16]. Wang et al. [17] used a modified version of Buongiorno's model to investigate heat, mass transfer of an Ag-H2O nano-thin film travelling through permeable media. Nasir et al. [18] investigated the flow of non-Newtonian BNF over a stretching surface within a non-Darcy porous medium, employing the Maxwell viscoelastic model and (HAM). Their study accounted for non-Fourier heat conduction, non-Fickian diffusion, and convective heat transfer effects. They found that flow is influenced by rheological, buoyancy, and thermophoretic effects, while temperature, thermal BLT, and nanoparticle concentration depend on Prandtl number, relaxation, diffusion, and Schmidt number.

The examination of fluid motion induced by the influence of a magnetic field is known as magnetohydrodynamics**.** The importance of researching MHD flows stems from their frequent occurrence in nature. Applications in metallurgy, purification, MHD energy production, and chemical manufacturing portray the importance of MHD fluids [19]. A novel subset of multifunctional magnetic polymers has surfaced in recent times. They have magnetic particles incorporated in them that react to outside electromagnetic fields. The rheological characteristics of these intricately magnetically controlled colloids can be precisely adjusted at the nano or micro scale. By combining the properties of ordinary polymers with (MHD) or electrically conducting liquids, these substances also referred to as electro-conductive polymers (ECPs) and magnetoelectric polymers (MEPs) work successfully [20]. A magnetic field applied externally can be used to tailor the electro-active phases of coating material by suspending metallic conducting particles in polymers to meet specific requirements. In recent times, a range of advanced and complex functional magnetic polymers has been developed for various technological applications. Known as electro-conductive polymers (ECPs), these materials possess unique rheological characteristics and magnetohydrodynamic (MHD) properties. By including metallic conducting elements into the coating melt, which causes the material to undergo electro-active phases when exposed to an external magnetic field, these smart materials can be optimized to function efficiently [21]. These materials improve the prevention of corrosion and defect sealing purposes. This has led to the development of many complicated supplies, such as iron oxide magnetic nano-coatings, nickel/aluminum electroconductive foam coatings, and thin magnetic films composed of cobalt. Powerful magnetic fields were used by Moreira et al. [22] to create thin-film coatings over sizable spinning regions with uniformly smooth exteriors for biomedical applications. Shoaib et al. [23] investigated the temperature distribution of nanostructure materials in three-dimensional MHD HNF flow via soil.

Fluid dynamics research has entered a completely new realm with the addition of the *"dissipative effect"*. Many researchers have also looked closely at how dissipation affects fluid movements. The process by which a fluid accomplishes work and subsequently turns into heat is known as viscous dissipation. "Viscous dissipation refers to the conversion of kinetic energy into thermal energy through frictional forces. It plays a significant role in influencing conventional convective processes across various systems. A comprehensive understanding and control of viscous dissipation are essential for enhancing the efficiency of systems utilizing (NFs), especially in applications that demand effective heat transfer and thermal regulation". Ramana et al. [24] presented the MHD dissipative Newtonian fluid non-Darcy flows past an axisymmetric surface with a heat source using the bvp4c technique. Reddy and Gaffar [25] have discussed an inclined plane's chemically viscous dissipative BNF transport while taking thermophoresis effects and Brownian movement into account. Shahzad et al. [26] explored the effects of Joule heating and viscous dissipation on the unstable magnetohydrodynamic (MHD) heat transfer of Jeffrey NF over a stretching sheet. Meanwhile, Awais et al. [27] examined the influence of bio-convective nanomaterials, considering factors such as heat immersion, stratification, and viscous dissipation.

Most fluid motions are depicted naturally in both similar and non-similar ways, with highly useful applications in terms of various flow topologies. Similar solutions each have a unique application sector. The flow of fluid close to the surface is another area that has been brought in for technical use. Examples include the production of glass fibre, wire drawing, paper, melting spinning, and rubber sheet and polymer extraction and manufacturing. Nevertheless, because of its intricate topological coordinates, this research is not appropriately taken into effect. In this context, Sparrow et al. [28] applied the non-similar flow characteristics to analyze flows dominated by viscous forces in specific regions. In a similar vein, Sparrow and Yu [29] investigated the non-similar traits of the boundary layer (BL), employing the heat balance framework to examine the thermal dynamics within the same domain. Non-similar transformations are mathematical techniques for analyzing fluid flow problems where flow variables like velocity, temperature, or concentration vary across the flow field without maintaining a consistent pattern. They introduce new variables to capture these variations, enabling the study of complex flows with non-uniform boundary conditions or geometries. This approach helps resolve fluid dynamics issues where a single dimensionless form cannot describe the entire flow. The significance of Newtonian liquid non-similar flow was first investigated by Minkowycz and Sparrow [30], who also came to some extremely important conclusions regarding the incorporation of stream-wise coordinates in the issue formulation. These methods are crucial for accurately modeling and solving real-world fluid flow scenarios that exhibit non-uniform pattern. Non-similar flows are crucial both theoretically and practically in heat transmission and BL flow, especially when material properties vary. These flows arise when transformations cannot fully resolve the dependence of independent variables, leading to differences in fundamental flow values along the streamwise direction. Appropriate transformations help simplify the altered equations, analyzing complex flow fields feasible. Some factors, including alterations in the freestream speed, differences in the temperatures of the heated wall, the consequences of injecting fluid or suction outdoors, surface transfer of mass, etc., can result in non-similarity. The Oldroyd-B fluid flow over an expanding surface is analysed using non-similar forced convection has been researched by Razzaq and Farooq [31] and they examined non-similar description and simulation of the Casson fluid's Darch-Forchheimer Brinkman challenge in a medium with pores were reported. Cross nanomaterials over a gravitationally affected surface were the subject of non-similar mathematical and dynamical analyses by Al Salami et al. [32]. A non-similar study of forced convection radially magnetised ternary hybrid flow NF on a curved stretched surface was examined by Jan et al. [33].

In the present work, motivated by coating applications involving magnetic NFs, an analytical model is developed for steady-state laminar BL flow of a magnetized BNF from a non-isothermal semi-infinite vertical plate to non-Darcy porous medium with, Lorentz forces, viscous dissipation, heat and mass transfer of NPs is considered. "Previous studies on NF flow and heat transfer have largely focused on classical fluid models and often neglected the combined influence of magnetic dissipation effects, thermophoresis, Brownian motion, and porous medium characteristics, particularly in the context of non-Darcy flow regimes. Additionally, the BNF model which accounts for nanoparticle movement due to thermophoresis and Brownian diffusion has rarely been applied in settings involving semi-infinite plates, non-Darcy porous media, and magneto-hydrodynamic (MHD) effects simultaneously. This research fills key gaps by using the Keller Box method to analyze non-similar convection flows, which are more realistic but less studied than similar flows. Using Buongiorno's nanofluid, it incorporates the (Da-Fs) model for the porous medium to account for inertial effects in high-velocity porous media flows. The primary objective of this study is to develop a rigorous mathematical framework for investigating the heat and mass transfer characteristics of BNF flow influenced by magneto-dissipative effects. The analysis is conducted over a semi-infinite vertical plate embedded in a non-Darcy porous medium, incorporating the impacts of Brownian motion and thermophoresis. This work seeks to elucidate the complex interplay between magnetic fields, porous medium resistance, and nanoparticle dynamics under non-linear flow regimes. The novelties of the present work are the simultaneous consideration of substrate (wall) non-isothermal semi-infinite vertical plate, (Da-Fs) drag, MHD, and viscous dissipation also partial differential equations which include fully two-dimensional Buongiorno's magnetic nanofluid coating flow. The dimensionless nonlinear multi-physical boundary value problem (BVP) with related wall and free stream boundary conditions is solved using the robust second-order accurate KBM. Validation with previous studies has been documented in the literature, authentication is accomplished, and error analysis is also performed. Velocity, temperature, and concentration distributions are computed and visualized graphically the "simulations are relevant to further deepening understanding of transport characteristics in magnetic nano-material manufacturing coating flows to enhance the design and optimization of cooling systems, electronic thermal management, and energy systems by providing accurate predictions of heat transmission, and fluid flow patterns. This research is particularly valuable for improving efficiency and performance in applications where precise thermal control and advanced fluid dynamics are critical and precise forecasts of heat, mass transfer, and fluid flow patterns by examining these intricate relationships".

A laminar, steady-state, incompressible convection flow of NF past a semi-infinite plate in an (x, y) coordinate system is studied, as illustrated in Figure 1 semi-infinite vertical plate is followed by *x-axis* going higher, and *y-axis* going normal to the plate. Buoyancy effects are often caused by gradients in a dispersed species' thermal region, which drives the flow. The flow over the horizontal sheet described by Navier-Stokes becomes identical to boundary-layer equations as the characteristic value of natural convection, or the Grashof number (Gr), is increased indefinitely. Gravitational acceleration (g) exerts a downward force. Both NF and semi-infinite plate are first kept constant in terms of both temperature and concentration. Additionally, the fluid temperature and concentration are raised to the ambient levels $T_W > T_\infty$, and remain fixed. To approximate the conductivity, a homogeneous and isotropic porous media is considered.

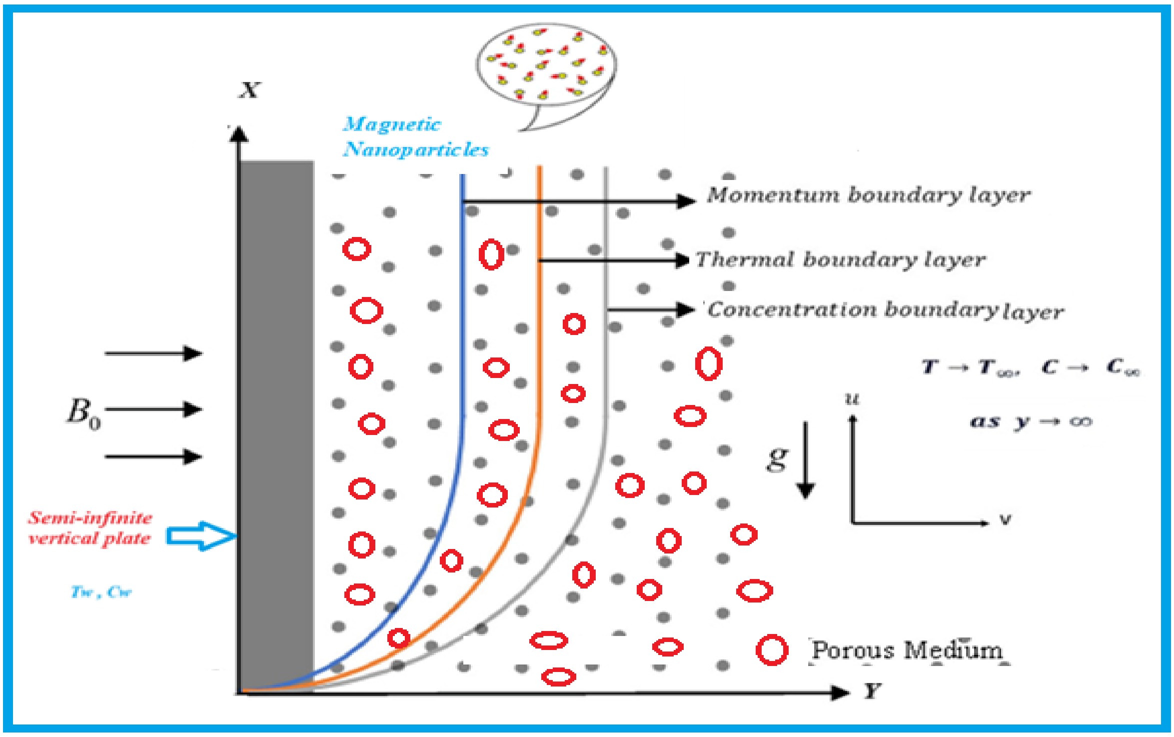

Figure 1. Magnetic nanofluid coating boundary layer model and coordinate system

2. MATHEMATICAL FORMULATION

To approximate the conductivity, a homogeneous and isotropic porous media is considered. The second order (Da-Fs) model's pressure gradient is described in the following way:

$$\nabla_p = -aU + bU^2 \tag{1}$$

where, ∇_p is the pressure, $a = \frac{\mu}{K}$ *and* $b = \frac{\rho}{K_1}$ are the constants and U is the velocity.

The governing equations for mass, momentum, energy, and nanoparticle species (concentration) for the BNF under the boundary layer and Boussinesq approximations may be established using the models of Buongiorno [3], Ramesh Reddy et al. [25, 34], Gaffar et al. [35], Ramya et al. [36], Anjum et al. [37], and Prasad et al. [38]. The vectorial forms of the conservation equations are:

$$\nabla . \boldsymbol{V} = 0 \tag{2}$$

$$\begin{aligned}\rho_f\left(\frac{\partial v}{\partial t} + V.\nabla V\right) &= -\nabla p + \mu_f(\nabla^2 V) \\ &+ g\left[(1 - C_\infty)\rho_{f\infty}(T - T_\infty)\beta \right. \\ &\left. - (\rho_p - \rho_{f\infty})(C - C_\infty)\right] - \frac{\sigma B2_0}{\rho}u\end{aligned} \tag{3}$$

$$\begin{aligned}(\rho c)_m\left(\frac{\partial T}{\partial t} + V.\nabla T\right) \\ &= k_m \nabla^2 T \\ &+ (\rho c)_m\left[D_B \nabla C.\nabla T + \frac{D_T}{T_\infty}(\nabla T)^2\right] \\ &+ \frac{v}{\rho C_p}(\nabla V)^2\end{aligned} \tag{4}$$

$$\frac{\partial C}{\partial t} + \frac{1}{\varepsilon}V.\nabla C = D_B \nabla^2 C + \frac{D_T}{T_\infty}\nabla^2 T \tag{5}$$

All the terms are discussed in the nomenclature. Here, *V=(u, v)* is the velocity vector.

The Semi-infinite substrate surface (wall) and free stream (BL edge) are subject to the following BCs Anjum et al. [37]:

$$u = v = 0, T = T_w, C = C_w \, at \, y = 0$$
$$u \to 0, T \to T_\infty, C \to C_\infty \, as \, y \to \infty \tag{6}$$

According to Kuznetsov and Nield [39], Eq. (3) may be expressed using the Oberbeck-Boussinesq approximations when the nanoparticle concentration is minimal, and the right pressure option is used. This results in the linearised momentum equation, which is as outlined below:

$$0 = -\nabla p + \mu_f(\nabla^2 V) + g\left[(1 - C_\infty)\rho_{f\infty}\beta(T - T_\infty) - (\rho_p - \rho_{f\infty})(C - C_\infty)\right] \tag{7}$$

The following are the simplified BL conservation equations for the present regime in a *(x,y)* coordinate framework:

$$\frac{\partial u}{\partial x} + \frac{\partial v}{\partial y} = 0 \tag{8}$$

$$u\frac{\partial u}{\partial x} + v\frac{\partial u}{\partial y} = \nu\frac{\partial^2 u}{\partial y^2} + g\left[(1 - C_\infty)\rho_{f\infty}\beta(T - T_\infty) - (\rho_p - \rho_{f\infty})(C - C_\infty)\right] - \frac{\nu}{K}u - \frac{b}{K}u^2 - \frac{\sigma B_0^2}{\rho}u \tag{9}$$

$$u\frac{\partial T}{\partial x} + v\frac{\partial T}{\partial y} = \alpha_m\frac{\partial^2 T}{\partial y^2} + \tau\left[D_B\frac{\partial T}{\partial y}\frac{\partial C}{\partial y} + \frac{D_T}{T_\infty}\left(\frac{\partial T}{\partial y}\right)^2\right] + \frac{\nu}{\rho C_p}\left(\frac{\partial u}{\partial y}\right)^2 \tag{10}$$

$$\frac{1}{\varepsilon}\left(u\frac{\partial C}{\partial x} + v\frac{\partial C}{\partial y}\right) = D_B\frac{\partial^2 C}{\partial y^2} + \frac{D_T}{T_\infty}\frac{\partial^2 T}{\partial y^2} \tag{11}$$

where,

$$\alpha_m = \frac{k_m}{(\rho c)_f}, \tau = \frac{(\rho c)_p}{(\rho c)_f} \tag{12}$$

ψ are defined as $u = \frac{\partial\psi}{\partial y}$ and $v = -\frac{\partial\psi}{\partial x}$

Subject to the velocity components given in terms of stream function, Eq. (8) is automatically met. The non-dimensional scaling parameters listed below are introduced [25, 35, 37]:

$$\xi = \left(\frac{x}{L}\right)^{\frac{1}{2}}, \quad \eta = C_1 y x^{-\frac{1}{4}}, \quad \psi = 4\nu C_1 x^{\frac{3}{4}} f(\xi,\eta), \quad C_1 = \left(\frac{Gr}{4}\right)^{\frac{1}{4}} L^{\frac{-3}{4}}$$
$$Gr = \frac{g\beta(1-C_\infty)\rho_{f\infty}(T_w - T_\infty)L^3}{4\nu^2}, \quad \theta(\xi,\eta) = \frac{T - T_\infty}{T_w - T_\infty}, \ \phi(\xi,\eta) = \frac{C - C_\infty}{C_w - C_\infty} \tag{13}$$

All parameters are defined in the nomenclature. Eqs. (9)-(11) are thus transformed into the subsequent system of interdependent, nonlinear equations. ODEs by virtue of the transformations from Eq. (13):

$$f''' + 3ff'' - 2f'^2 + (\theta - Nr\phi) - \frac{\xi}{DaGr^{\frac{1}{2}}}f' - \frac{Fs}{Da}\xi^2 f'^2 - M\xi f' = 2\xi\left(f'\frac{\partial f'}{\partial \xi} - f''\frac{\partial f}{\partial \xi}\right) \tag{14}$$

$$\frac{\theta''}{\Pr} + 3f\theta' + Nb\theta'\phi' + Nt\theta'^2 + Ec\xi^2 f''^2 = 2\xi\left(f'\frac{\partial\theta}{\partial\xi} - \theta'\frac{\partial f}{\partial\xi}\right) \tag{15}$$

$$\frac{\phi''}{Sc} + 3f\phi' + \frac{1}{Sc}\frac{Nt}{Nb}\theta'' = 2\xi\left(f'\frac{\partial\phi}{\partial\xi} - \phi'\frac{\partial f}{\partial\xi}\right) \tag{16}$$

The transformed non-dimensional BCs are:

$$f = 0, \quad f' = 0, \quad \theta = 1, \quad \phi = 1 \quad at \ \eta = 0$$
$$f' \to 0, \quad \theta \to 0, \quad \phi \to 0 \quad as \ \eta \to \infty \tag{17}$$

Here the following non-dimensional quantities are introduced:

$$Nr = \frac{(\rho_p - \rho_{f\infty})(C_w - C_\infty)}{\rho_{f\infty}(1 - C_\infty)\beta(T_w - T_\infty)}, Nb = \frac{\tau D_B(C_w - C_\infty)}{\nu}, \ Nt = \frac{\tau D_T(T_w - T_\infty)}{\nu T_\infty}$$
$$Da = \frac{K}{2L^2}, \ Fs = \frac{2b}{L}, \Pr = \frac{\nu}{\alpha_m}, \ Sc = \frac{\nu}{D_m\varepsilon}, M = \frac{\sigma B_0^2 L^{\frac{1}{2}}}{\mu C_1^2}, \ Ec = \frac{16\nu^2 C_1^4 L}{\rho C_p(T_w - T_\infty)} \tag{18}$$

Here all parameters are defined in the nomenclature. The shear stress components at the surface, known as the skin-friction coefficients (C_f), the heat transfer rate known as Nusselt number (*Nu*), and the mass transfer rate of NPs, known as the Sherwood number (*Sh*), are the physically key interesting engineering design parameters for the Semi-infinite vertical surface. They are defined as follows:

$$C_f = 4\nu\mu C_1^3 x^{\frac{1}{4}} f''(\xi,0) \tag{19}$$

$$Nu = -k\Delta T C_1 x^{\frac{-1}{4}}\theta'(\xi,0) \tag{20}$$

$$Sh = -D\Delta C\, C_1 x^{\frac{-1}{4}}\phi'(\xi,0) \tag{21}$$

$$\frac{1}{4\nu\mu C_1{}^3 x^{\frac{1}{4}}}C_f = f''(\xi,0) \tag{22}$$

$$\frac{-1}{k\Delta T C_1 x^{\frac{-1}{4}}}Nu = \theta'(\xi,0) \tag{23}$$

$$\frac{-1}{D\Delta C\, C_1 x^{\frac{-1}{4}}}Sh = \phi'(\xi,0) \tag{24}$$

$$\Delta T = T_w - T_\infty, \quad \Delta C = C_w - C_\infty$$

Here, $\xi \sim 0$ and the BLEs (14)-(16) contract to a system of ODEs in the neighbourhood of the lower stagnation point:

$$f''' + 3ff'' - 2f'^2 + (\theta - Nr\phi) - \frac{\xi}{DaGr^{\frac{1}{2}}}f' - \frac{Fs}{Da}\xi^2 f'^2 - M\xi f' = 0 \tag{25}$$

$$\frac{\theta''}{\Pr} + 3f\theta' + Nb\theta'\phi' + Nt\theta'^2 + Ec\xi^2 f''^2 = 0 \tag{26}$$

$$\frac{\phi''}{Sc} + 3f\phi' + \frac{1}{Sc}\frac{Nt}{Nb}\theta'' = 0 \quad (27)$$

3. KELLER BOX COMPUTATION SOLUTION AND VALIDATION

The dimensionless BLEs (14)-(16), along with the boundary condition (17), have been numerically resolved through the implementation of the Keller box implicit finite difference method [40]. This method remains one of the best numerical techniques for solving two-point BVPs. The Keller-box approach offers appealing extrapolation properties and second-order accuracy with flexible spacing. On a rectangular grid Figure 2, a finite-difference technique is used ("box") and converts partial differential equations of the BL into an algebraic set of equations. It attains remarkable accuracy, offers steady numerical meshing characteristics, and converges quickly. By utilizing fully implicit methods with customizable stepping, KBM improves accuracy on explicit or semi-implicit schemes. Another advantage of this method is that two-coordinate (ξ, η) nonlinear partial differential equation systems can be easily accommodated, unlike other solvers such as MATLAB BVP4C, which are restricted to ordinary differential BVPs. Originally formulated by Keller [40] for analyzing low-velocity aerodynamic BLs, this technique has since been widely adopted across a broad spectrum of industrial Multiphysics fluid dynamics applications. These encompass radiative-convective magnetohydrodynamic flow over curved geometries within porous structures [35], micropolar convective phenomena [41], as well as transient viscoelastic fluid motion and associated mass transport processes. Consistent with the underlying principles of parabolic systems, each discretization interval is entirely interlinked, ensuring comprehensive coupling of the governing variables at every computational step. The discrete algebra connected to the KBM technique is essentially independent of any other mimicking (physics-capturing) computation methods [42-44]. Recent applications of this method in multi-physical coating flows include the thermo-rheological coating flow of a cone [45] and the non-Newtonian enrobing flow of a cylinder [46].

The four phases involved in the KBM are:

1) Splitting the system of N^{th} order PDEs down to *the N first* order ODEs.
2) Finite Difference Discretization.
3) Quasi-linearization of Non-Linear Keller Algebraic Equations.
4) Block-tridiagonal elimination solution of the Linearized Keller Algebraic Equations.

Step1: Reduction of the Nth order partial differential equation system to N first order equations

Eqs. (18)-(20) and boundary conditions (21), in conjunction with the introduction of auxiliary variables, are utilized to reformulate the BVP into a system comprising multiple first-order differential equations. Consequently, the incorporation of these new variables yields a system of nine concurrently solvable first-order ordinary differential equations.

$$u(x,y) = f', v(x,y) = f'', g'(x,y) = p, s(x,y) = \theta, t(x,y) = \theta' \quad (28)$$

$$f' = u \quad (29)$$

$$u' = v \quad (30)$$

$$g' = p \quad (31)$$

$$s' = t \quad (32)$$

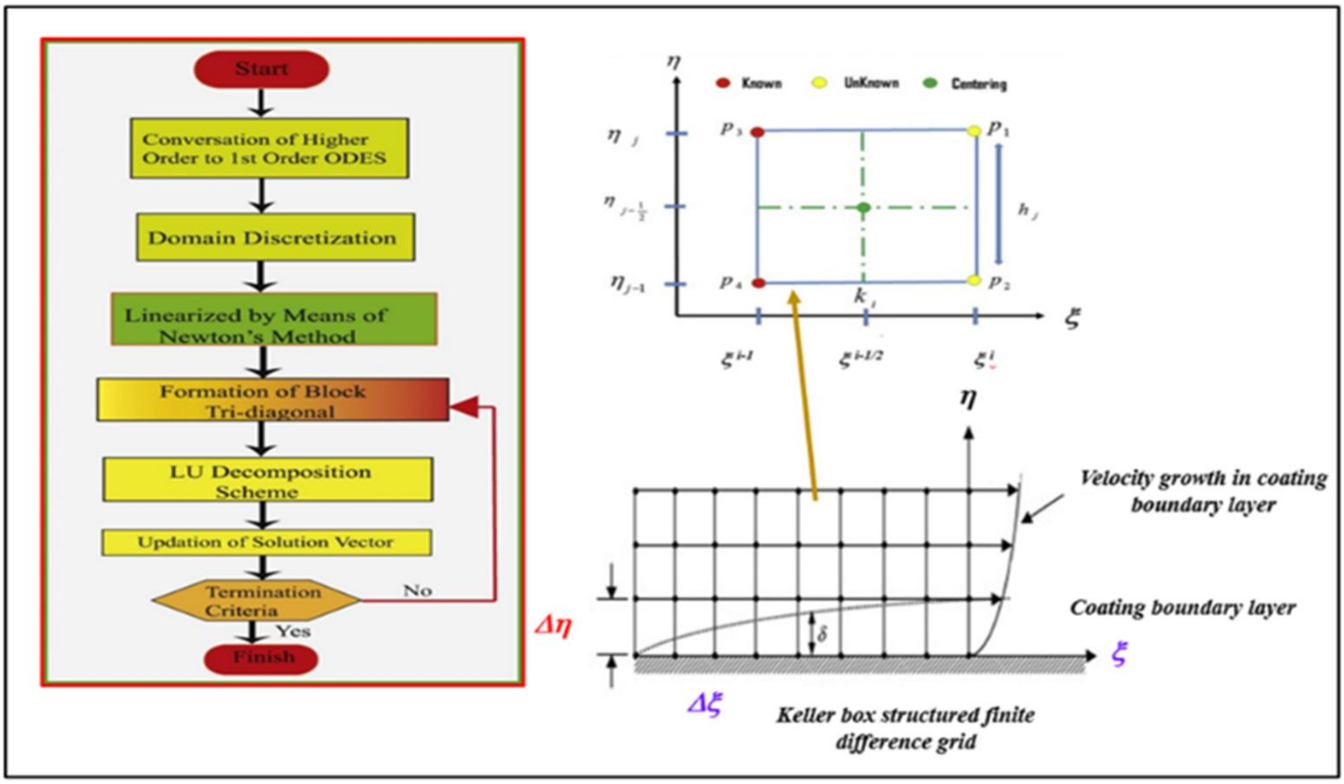

Figure 2. Keller box procedure, box cell and boundary layer meshing

$$v' + 3fv - 2u^2 + (s - Nrg) - \left(\frac{\xi}{Da\sqrt{Gr}} + M\xi\right)u - \frac{Fs}{Da}\xi^2u^2 = 2\xi\left[u\frac{\partial u}{\partial \xi} - v\frac{\partial f}{\partial \xi}\right] \tag{33}$$

$$\frac{t'}{\Pr} + 3ft + Nbt\,p + Nt\,t^2 + Ec\,\xi^2 v^2 = 2\xi\left(u\frac{\partial s}{\partial \xi} - t\frac{\partial f}{\partial \xi}\right) \tag{34}$$

$$\frac{p'}{Sc} + \frac{1}{Sc}\frac{Nt}{Nb}t' + 3fp = 2\xi\left(u\frac{\partial g}{\partial \xi} - p\frac{\partial f}{\partial \xi}\right) \tag{35}$$

Here, the prime notation signifies differentiation with respect to the independent variable η. Expressed in terms of the dependent variables, the BCs are reformulated as follows:

$$\begin{aligned} &f = 0, \quad f' = 0, \quad \theta = 1, \quad \phi = 1 \quad at \quad \eta = 0 \\ &f' \to 1, \quad \theta \to 0, \quad \phi \to 0 \quad\quad as \quad \eta \to \infty \end{aligned} \tag{36}$$

Step 2: Finite Difference Discretization

Within a Keller box framework (computational cell), a two-dimensional numerical mesh is established over the ξ–η coordinate plane. The advancement procedure is characterized by the following stepwise formulation:

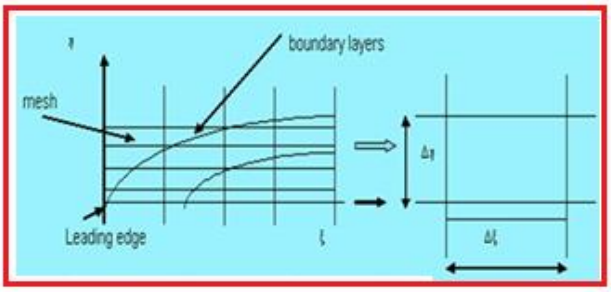

2-Dimensional computational grid on the ξ–η plane

$$\eta_0 = 0, \quad \eta_j = \eta_{j-1} + h_j, \quad j = 1,2,\ldots,J, \quad \eta_J \equiv \eta_\infty \tag{37}$$

$$\xi^0 = 0, \quad \xi^n = \xi^{n-1} + k_n, \quad n = 1,2,\ldots,N \tag{38}$$

where, k_n is the $\Delta\xi$ -spacing and h_j is the $\Delta\eta$ -spacing. If g_j^n denotes the value of any variable at (η_j, ξ^n), then the variables and derivatives of Eqs. (28)-(35) at $(\eta_{j-1/2}, \xi^{n-1/2})$ are replaced by:

$$g_{j-1/2}^{n-1/2} = \frac{1}{4}\left(g_j^n + g_{j-1}^n + g_j^{n-1} + g_{j-1}^{n-1}\right) \tag{39}$$

$$\left(\frac{\partial g}{\partial \eta}\right)_{j-1/2}^{n-1/2} = \frac{1}{2h_j}\left(g_j^n - g_{j-1}^n + g_j^{n-1} - g_{j-1}^{n-1}\right) \tag{40}$$

$$\left(\frac{\partial g}{\partial \xi}\right)_{j-1/2}^{n-1/2} = \frac{1}{2k^n}\left(g_j^n - g_{j-1}^n + g_j^{n-1} - g_{j-1}^{n-1}\right) \tag{41}$$

The resulting finite-difference approximation of Eqs. (28)-(35) for the mid-point $(\eta_{j-1/2}, \xi^n)$, are:

$$h_j^{-1}\left(f_j^n - f_{j-1}^n\right) = u_{j-1/2}^n \tag{42}$$

$$h_j^{-1}\left(u_j^n - u_{j-1}^n\right) = v_{j-1/2}^n \tag{43}$$

$$h_j^{-1}\left(g_j^n - g_{j-1}^n\right) = p_{j-1/2}^n \tag{44}$$

$$h_j^{-1}\left(s_j^n - s_{j-1}^n\right) = t_{j-1/2}^n \tag{45}$$

$$\begin{aligned} &(v_j - v_{j-1}) + \frac{h_j}{4}(3+2\alpha)(f_j + f_{j-1})(v_j + v_{j-1}) \\ &\quad + \frac{h_j}{2}\left(s_j + s_{j-1} - Nr(g_j + g_{j-1})\right) \\ &-2\left(1 + \alpha - \frac{Fs}{Da}\xi^2\right)\frac{h_j}{4}(u_j + u_{j-1})^2 \\ &\quad - \left(\frac{\xi}{Da\sqrt{Gr}} + M\xi\right)\frac{h_j}{2}(u_j + u_{j-1}) \\ &\quad - \alpha h_j f_{j-1/2}^{n-1}(v_j + v_{j-1}) \\ &-\alpha h_j v_{j-1/2}^{n-1}(f_j + f_{j-1}) - v^{n-1} = [R_1]_{j-/12}^{n-1} \end{aligned} \tag{46}$$

$$\begin{aligned} &\frac{1}{Pr}(t_j - t_{j-1})\frac{h_j}{4}(3+2\alpha)(f_j + f_{j-1})(t_j \\ &\quad + t_{j-1})\frac{h_j}{4}(t_j + t_{j-1})(p_j \\ &\quad + p_{j-1})\frac{h_j}{4}(t_j + t_{j-1})^2 \\ &\quad - 2\frac{\alpha h_j}{4}(su)_{j-1/2}^{n-1} \\ &\quad + \alpha h_j\left(s_{j-1/2}^{n-1}(u_j + u_{j-1})\right. \\ &\quad - u_{j-1/2}^{n-1}(s_j + s_{j-1}) \\ &\quad - f_{j-1/2}^{n-1}(t_j + t_{j-1}) \\ &\quad \left. + t_{j-1/2}^{n-1}(f_j + f_{j-1})\right) \\ &\quad + Ec^2\xi^2(v_j + v_{j-1})^2 = [R_2]_{j-1/2}^{n-1} \end{aligned} \tag{47}$$

$$\begin{aligned} &\frac{1}{Sc}(p_j - p_{j-1}) + \frac{1}{Sc}\frac{Nt}{Nb} \\ &\quad + \frac{h_j}{4}(3+2\alpha)(f_j + f_{j-1})(p_j \\ &\quad + p_{j-1}) \\ &\quad + 2\frac{\alpha h_j}{2}\left(g_{j-1/2}^{n-1}(u_j + u_{j-1})\right. \\ &\quad - u_{j-1/2}^{n-1}(g_j + g_{j-1}) \\ &\quad - f_{j-1/2}^{n-1}(p_j + p_{j-1}) \\ &\quad \left. + p_{j-1/2}^{n-1}(f_j + f_{j-1})\right) \\ &\quad - 2\frac{\alpha h_j}{4}(ug)_{j-1/2}^{n-1} = [R_3]_{j-1/2}^{n-1} \end{aligned} \tag{48}$$

where, we have used the abbreviations:

$$\alpha = \frac{\xi^{n-1/2}}{k_n}$$

$$[R_1]_{j-1/2}^{n-1} = -h_j\left[\begin{array}{c} (v')_{j-\frac{1}{2}}^{n-1} + (3-2\alpha)(fv)_{j-\frac{1}{2}}^{n-1} \\ +\left(s_{j-1}^{n-1} - Nrg_{j-1}^{n-1}\right) - \left(\begin{array}{c} .\xi \\ \overline{Da\sqrt{Gr}} \\ +M\xi \end{array}\right)\left(u_{j-1}^{n-1}\right) + \\ \left(2 - 2\alpha - \frac{Fs}{Da}\right)\left(u_{j-1}^{n-1}\right)^2 \end{array}\right] \tag{49}$$

$$[R_2]_{j-1/2}^{n-1} = -h_j \begin{bmatrix} \dfrac{1}{Pr(t')_{j-\frac{1}{2}}^{n-1}(3-2\alpha)} \\ (ft)_{j-1/2}^{n-1}(tp)_{j-1/2}^{n-1}(t^2)_{j-1/2}^{n-1}{}^{2}(v^2)_{j-1/2}^{n-1} \\ +2\alpha(us)_{j-1/2}^{n-1} \end{bmatrix} \quad (50)$$

$$[R_3]_{j-1/2}^{n-1} = -h_j \left[\frac{1}{Sc}(p')_{j-1/2}^{n-1} + \frac{1}{Sc}\frac{Nt}{Nb}(t')_{j-1/2}^{n-1} + (3-2\alpha)(fp)_{j-1/2}^{n-1} + 2\alpha(ug)_{j-1/2}^{n-1} \right] \quad (51)$$

The BCs are:

$$f_0^n = 0,\ u_0^n = 0,\ g_0^n = 0,\ s_0^n = 0,\ u_J^n = 0,\ g_J^n = 0,\ s_J^n = 0 \quad (52)$$

Stage 3: Keller algebraic equations that are non-linear can be quasi-linearized.

If we presume $f_j^{n-1}, u_j^{n-1}, v_j^{n-1}, g_j^{n-1}, p_j^{n-1}, s_j^{n-1}, t_j^{n-1}$ to be widely recognized for $0 \le j \le J$, the consequence is in a framework of *7J+7* equations for the solution of *7J+7* unknowns $f_j^n, u_j^n, v_j^n, g_j^n, p_j^n, s_j^n, t_j^n$ $j = 0,1,2,\ldots,J$. This non-linear system of algebraic equations is linearized by means of Newton's method.

Stage 4: The linearized Keller Algebraic Equations' block-tridiagonal elimination solution.

Since the linearized system has a block-tridiagonal structure, it is solved using the block-elimination technique. This results in a block-tridiagonal architecture composed of block matrices. Every component of the coefficient matrix is a matrix in and of itself, and the full linearized system is represented as a block matrix framework. This system is solved using the efficient Keller-box approach. A significant influence on the numerical output is the quantity of mesh points in both axes. After a few experiments, A greater density of grid points is chosen within the computational domain radial coordinate (η-direction), whereas a significantly lesser number are employed in the tangential coordinate (ξ-direction). η_{max}=16 establishes an appropriately high level at which the desired BCs are accomplished. For this flow domain, ξ_{max} is set as 3. In the current computation, mesh independence is attained. The computational algorithm is run on a PC using MATLAB. As explained by Keller [45], the procedure exhibits outstanding stability, convergence and consistency.

3.1 Convergence analysis

Until a certain convergence threshold is met, computations are performed. Laminar boundary-layer calculations commonly use the wall shear stress parameter, $v(\xi, 0)$, as the convergent standards [47]. The most significant error in BL calculations is found to be in the parameter of wall shear stress. Noteworthy is the fact that this convergence criteria is used throughout the study since it is effective, appropriate, and the best solution to all of the issues taken into consideration. The computations are terminated when $\left|\delta v_0^{(i)}\right| \prec \varepsilon_1$, a modest $\varepsilon_1$specified value is reached. ε_1=0.00001, which provides an accuracy of around 4 decimal places for anticipated amounts in this investigation.

3.2 Validation of Keller box code

(*Nu*) and (C_f) for various values of *Gr* are contrasted with those found in prior investigations to evaluate the current numerical code's authenticity. Table 1 and the Figure 3 exhibit this by comparing the validity of the current research to previous investigations by Plumb and Huenefeld [48] and Chamkha et al. [49]. Table 2 and Figure 4 provide local skin friction coefficient (C_f) results that are contrasted with Newtonian solutions provided by Reddy et al. [34], Merkin and Pop [50], and Sadiqa et al. [51] for various values of ξ and excellent agreement is achieved. The reliability of the current Keller box code is confirmed by the very precise concurrence obtained based on the latest and most recent data. The data shows significant consistency and dependability in the observed patterns, confirming that the current results support and strengthen the outcomes of previous analyses. Error analysis percentage of the comparisons are also included.

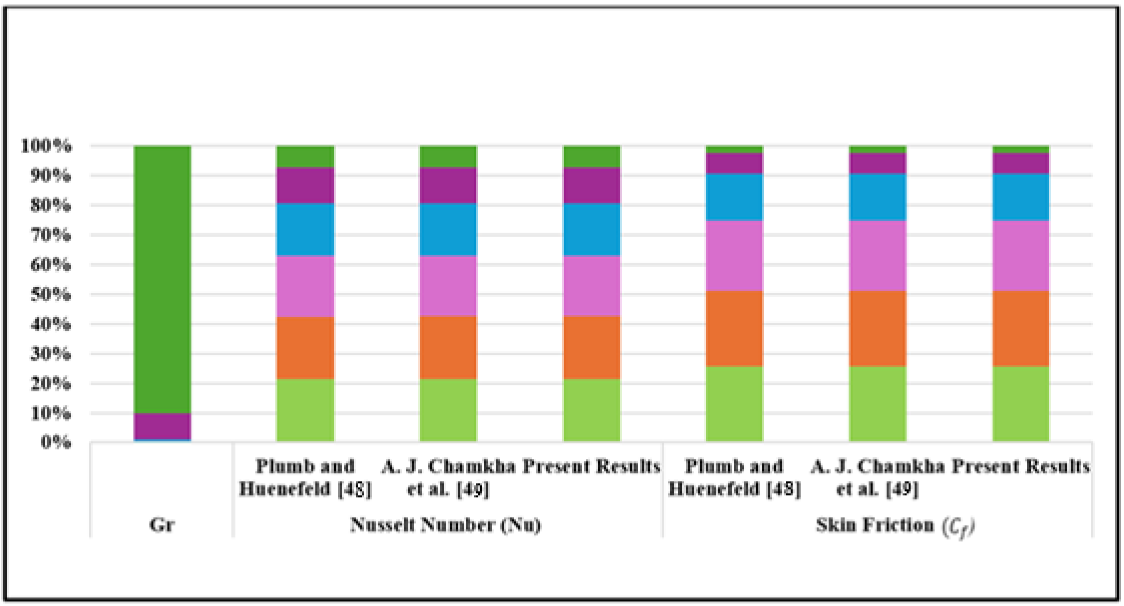

Figure 3. Bar graph for the comparison of (*Nu*), (C_f) for various values of *Gr*

Table 1. Comparison of dimensionless (Nu), (C_f) for various values of Gr

Gr	Nusselt Number (Nu)			Skin Friction (C_f)		
	Plumb and Huenefeld [48]	Chamkha et al. [49]	Present Results	Plumb and Huenefeld [48]	Chamkha et al. [49]	Present Results
0	0.4439	0.44374	0.44372	1	1	1
0.01	0.44232	0.44216	0.44219	0.9902	0.99019	0.99017
0.1	0.42969	0.4295	0.4291	0.91608	0.91608	0.91603
1	0.36617	0.36575	0.36579	0.61803	0.61803	0.61805
10	0.25126	0.25065	0.25067	0.27016	0.27016	0.27015
100	0.15186	0.15145	0.15143	0.09512	0.09512	0.09516

Table 2. Local skin friction coefficient (C_f) comparison for different values of ξ *as* $Da \to \infty$, Fs=0

Skin Friction Coefficient (C_f)							
ξ	Ramesh Reddy et al. [34]	Merkin and Pop [50]	Saddiqa et al. [51]	Current Results	Error Analysis% with [34]	Error Analysis% with [50]	Error Analysis% with [51]
0.1	0.012	0.014	0.014	0.016	4%	2%	2%
0.2	0.049	0.051	0.050	0.054	5%	3%	4%
0.3	0.103	0.105	0.104	0.106	3%	1%	2%
0.4	0.171	0.172	0.172	0.169	2%	3%	3%
0.5	0.249	0.250	0.250	0.251	2%	1%	1%
0.6	0.338	0.337	0.336	0.339	1%	2%	3%
0.7	0.429	0.430	0.430	0.432	3%	2%	2%
0.8	0.528	0.530	0.529	0.531	3%	1%	2%
0.9	0.634	0.635	0.634	0.634	0%	1%	0%
1	0.743	0.745	0.744	0.747	4%	2%	3%
1.1	0.857	0.859	0.858	0.860	3%	2%	2%
1.2	0.971	0.972	0.975	0.975	4%	3%	0%
1.4	…	…	…	0.998			

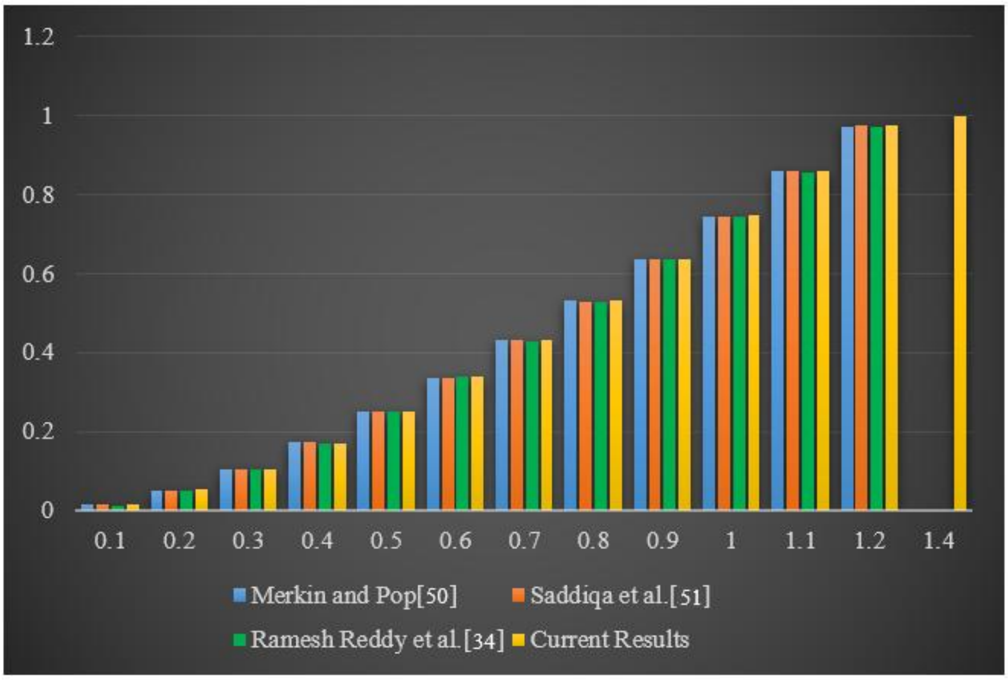

Figure 4. Bar graph for the comparison of (C_f) for different ξ values

4. GRAPHICAL AND TABULAR RESULTS AND DISCUSSIONS

The mathematical viewpoint of BNF's flow via a semi-infinite vertical plate with a non-Darcy-porous material is highlighted in this section of the paper. The KBM is applied for Eqs. (15)-(17). A detailed graphical illustration of the solution is shown in Figures 5-14 utilizing MATLAB code, on (f'), (θ), (ϕ), (C_f), (Nu), (Sh) for nine dimensionless thermophysical parameters in the model, such as (Nb), (Nt), (Nr), (Da), (Fs), (M), (Ec), (Sc), (Gr) are presented along the radial coordinate (η). The Numerical problem comprises two independent space variables (ξ, η), default values of the following variables are Pr=0.71, Sc=0.6, Nr=0.1, Nb=0.3, Nt=0.3, Da=Fs=M=Ec=0.5, Gr=10, ξ=1.0 are prescribed.

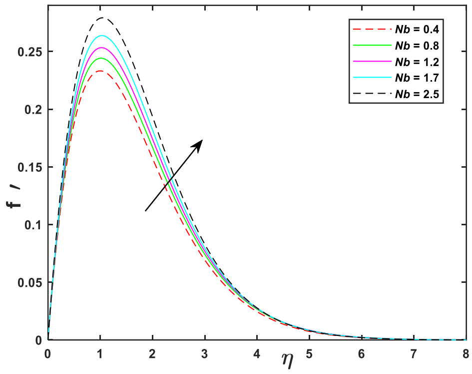

(a) Influence of Nb on velocity profile

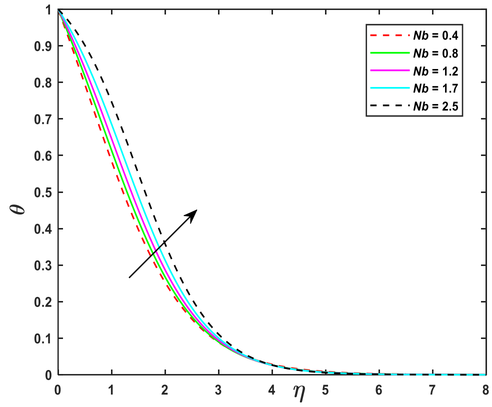

(b) Influence of Nb on temperature profile

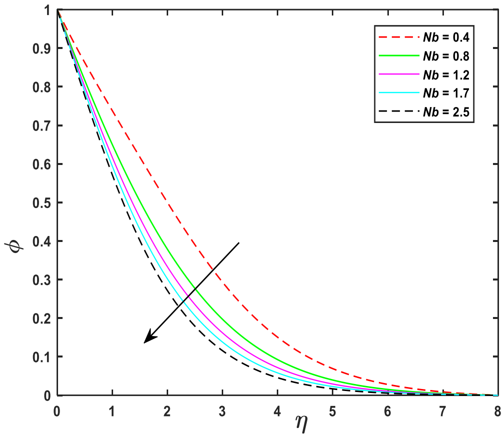

(c) Influence of Nb on concentration profile

Figure 5. Effect of Brownian diffusion parameter *Nb* on velocity, temperature and concentration profiles

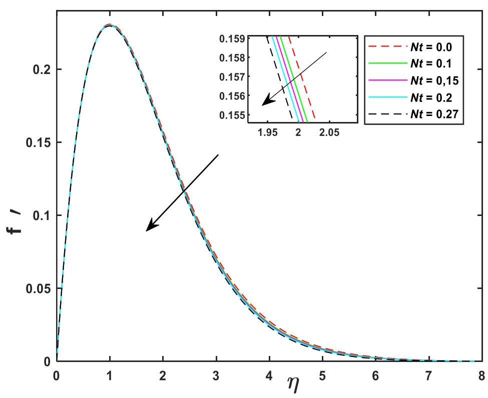

(a) Influence of Nt on velocity profile

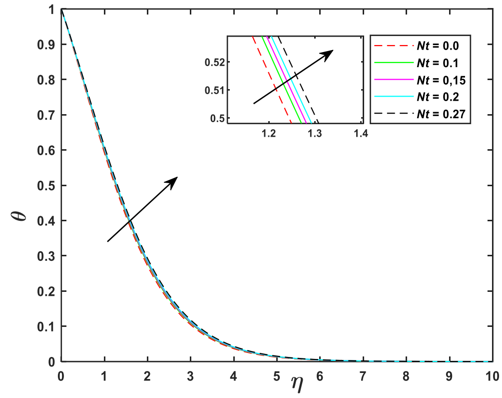

(b) Influence of Nt on temperature profile

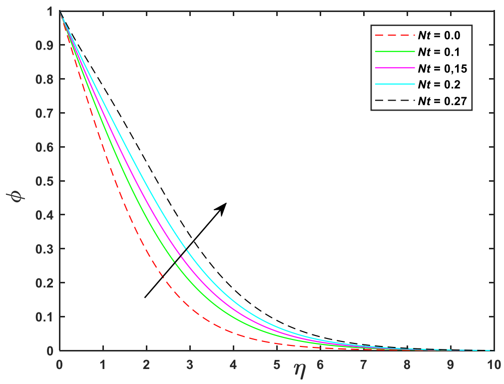

(c) Influence of Nt on concentration profile

Figure 6. Effect of thermophoresis parameter *Nt* on velocity, temperature and concentration profiles

Figures 5(a)-5(c) shows effect of Brownian diffusion, ($0.4 \le Nb \le 2.5$), on (f'), (θ), (ϕ) profiles. Mathematically, it can be expressed as: $Nb = \frac{\tau D_B(C_w - C_\infty)}{\nu}$. This term $+Nb\theta'\phi'$ appears in thermal Eq. (16) and $+\frac{Nt}{Nb}\frac{1}{Sc}\theta''$ appears in concentration Eq. (17). According to the Buongiorno formulation [3], higher values of *Nb* indicate smaller NPs, and varying this parameter produces a change in ballistic collisions. In Figure 5(a). (f') is enhanced although a stronger elevation is computed in the former with greater *Nb* values. (*Nb*) also modifies NF thermal conductivity and the propensity for heat transmission in the NF. As a result, the increased random motion of the NPs modifies the thermal pattern as well, and the momentum field experiences this influence through thermal buoyancy. As *Nb* increases, (θ) is positively affected across the BL regime, as seen in Figure 5(b). There is also a significant change in the topology of (θ) further from the substrate (wall) at very high *Nb* values. Raising (θ) aggravates the motion of the NPs and ballistic collisions. Consequently, chaotic (*Nb*) is increased even further. The increased heat conduction in the regime and the improved micro-convection surrounding the NPs are also influenced by the change in thermal conductivity with greater Brownian motion. This results in a thicker thermal BL due to a heating effect. Although the fluid's molecules and NPs are always moving, there is a noticeable shift in (θ) overall. Brownian motion, however, predominates in the random thermal motion of NPs. As *Nb* is increased, however, the intensification in ballistic collisions curtails the diffusion of NPs and this produces a notable decrease in (ϕ) values, as observed in Figure 5(c). Hence, the thickness of (ϕ) is reduced which is important in fine-tuning coating structure during the manufacturing process. Our findings align with the patterns observed in, Reddy et al. [25, 34], Ramya et al. [36], and Prasad et al. [38]. It has also been demonstrated that the increased viscosity enhances the flow and thermal convection, while simultaneously reducing the rates of mass transfer. The physical significance of these observations lies in the complex interplay between (*Nb*) and NF dynamics. As *Nb* increases, NPs experience enhanced random movement, facilitating more efficient thermal diffusion and accelerating (f'). This phenomenon is crucial in settings where efficient heat transport is necessary, like cooling structures and thermal management in engineering. However, the reduction in concentration gradient signifies a more homogeneous dispersion of NPs, which can affect processes reliant on localized concentrations, such as drug delivery or materials synthesis. The fluid's (*Nb*) is significantly impacted by increasing *Nb* levels because of the ' random NPs mobility.

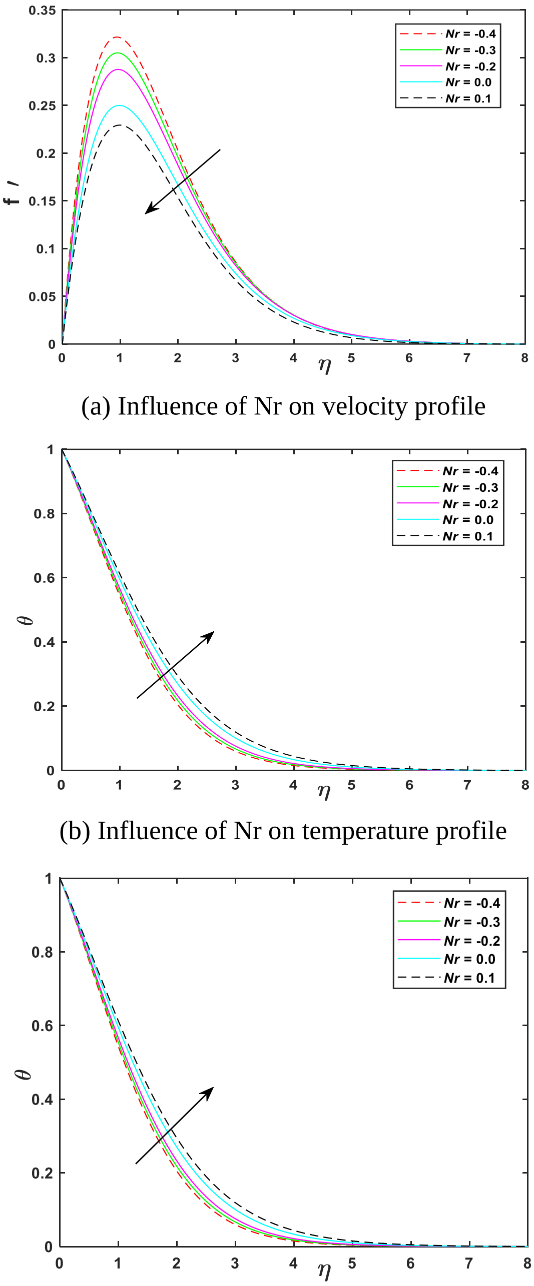

(a) Influence of Nr on velocity profile

(b) Influence of Nr on temperature profile

(c) Influence of Nr on concentration profile

Figure 7. Effect of buoyancy ratio parameter *Nr* on velocity, temperature and concentration profiles

Figures 6(a)-6(c) illustrate the effect of the thermophoretic parameter, ($0 \le Nt \le 0.27$) on (f'), (θ), (ϕ). Mathematically, it can be expressed as: $Nt = \frac{\tau D_T (T_w - T_\infty)}{\nu T_\infty}$. This term $+Nt\theta'^2$ appears in the thermal Eq. (16) and $+\frac{Nt}{Nb}\frac{1}{Sc}\theta''$ appears in the concentration Eq. (17). According to the Buongiorno formulation [3], thermophoretic body force has a direct impact on nanoparticle diffusion. From Figure 6(a) an increase in *Nt* decelerates (f'). The increasing thermophoresis parameter value enhances (θ) in Figure 6(b) and considerably boosts (ϕ) in Figure 6(c) These trends are sustained at all distances transverse to the inclined substrate. However, while asymptotic decays occur from the wall to the free stream for all (θ), (ϕ) profiles is only a decay for Nt=0, which has not been identified previously in the literature. With the subsequent elevation in the thermophoresis parameter, a peak in (ϕ) merges progressively further from the wall. Eventually, however, profiles for $Nt > 0.1$ do descend smoothly to the free stream. Overall, stronger thermophoresis elevates the thermal and nanoparticle species BLT, which inevitably influences the structure of the coating regime. The influence of an increased thermophoretic temperature gradient is pronounced across all transport properties, confirming the important role it plays in NF mechanics. Our findings support the patterns of Reddy et al. [25, 34], Ramya et al. [36], and Prasad et al. [38]. It has also been demonstrated that the higher viscosity serves to slow down the flow while enhancing both heat convection and mass transfer rates. Physically, this signifies that a stronger thermophoretic force leads to enhanced momentum, heat, and mass transfer, reflecting more pronounced thermal and solute gradients in NF flow. The two most intriguing aspects of Buongiorno's NF model are thermophoresis and Brownian motion characteristics. In essence, these characteristics raise (θ) which is essential for optimizing heat and mass transfer processes in various applications.

Figures 7(a)-7(c) elucidate the impact of the combined Buoyancy ratio parameter ($-0.4 \le Nr \le 0.1$) on profiles (f'), (θ), (ϕ). Dual natural convection currents mobilized by temperature and nanoparticle species are present. The combined buoyancy effect is simulated via the term, $+(\theta - Nr\phi)$, in the momentum Eq. (15) in which $Nr = \frac{(\rho_p - \rho_{f\infty})(C_w - C_\infty)}{\rho_{f\infty}(1 - C_\infty)\beta(T_w - T_\infty)}$. Buoyancy ratio parameter (*Nr*) quantifies the relative effect of thermal and concentration-driven buoyancy forces on fluid motion is characterized by the ratio of the concentration-induced buoyancy force to the thermal buoyancy force. The regime exhibits buoyancy from both thermal and nanoscale species, resulting in dual natural thermo-solute convection. For $Nr>0$, the flow is clearly accelerated (Figure 7(a)) at a certain distance from the plate surface. In contrast, when $Nr<0$, which represents the case where thermal and species buoyancy forces oppose one another, the flow experiences deceleration. As the distance from the plate surface increases, the effect of Nr undergoes a shift; for $Nr>0$, there is a slight decrease in the flow rate, whereas the opposite occurs for $Nr<0$. However, the impact of a significant change in *Nr* becomes less noticeable as one moves farther from the wall. If Nr=0, forced convection occurs, buoyancy forces disappear. Buoyancy forces thus have a considerably stronger influence near the surface of the plate. As seen in Figure 7(a), (f') is suppressed with positive *Nr* but is enhanced with negative *Nr*. In other words, assistive buoyancy damps the primary flow whereas opposing buoyancy. This reduction weakens buoyancy-driven movement, tending to a decrease in (f'). Consequently, with less buoyancy force driving fluid motion, the convective heat transfer process is hindered, resulting in depreciation of (f') profiles in the system. Temperature and concentration exhibit distinctly different reactions for varying values of *Nr*. As illustrated in Figures 7(b) and 7(c), in both scenarios, the opposition of buoyancy forces consistently increases the values across the entire BL region. When $Nr<1$, thermal buoyancy effects will prevail over concentration buoyancy, whereas for $Nr>1$, concentration buoyancy forces will dominate. Figures 7(b)-7(c) demonstrate that an increment of *Nr* strengthens the buoyancy-driven flows. This augmentation enhances fluid motion, facilitating more effective mixing and transport of heat and solute. Consequently, (θ), (ϕ) profiles are appreciated. Notably, both (θ), (ϕ) show an upward trend, signifying the heightened internal buoyancy forces improve heat, mass transfer. This results in higher thermal, solute gradients near the surface, causing increased (θ), (ϕ) levels within the boundary. Our outcomes align with the observed trends of Reddy et al. [25], Prasad et al. [38], and Gaffar et al. [42]. Physically, this signifies that stronger buoyancy effects lead to more efficient energy and species transport in the fluid this is essential for precisely estimating flow pattern maximizing mass and heat transfer in a variety of technical applications.

Figures 8(a)-8(c) portrays impact of Darcy number ($0.4\leq Da\leq 2.5$) on profiles (f'), (θ), (ϕ). Across the surface domain, along the transverse coordinate (η). Particularly in the study of flow via porous media, it's given by ratio of permeability of porous medium to characteristic length scale squared. This term $-\frac{\xi}{DaGr^{\frac{1}{2}}}f' - \frac{Fs}{Da}\xi^2 f'^2$ appears in momentum Eq. (15). Darcy number is employed to assess the relative impact of the porous medium's resistance to fluid movement in comparison to the inertial forces. A small Da value signifies that the flow is predominantly controlled by the resistance of the porous medium, whereas a large Da value indicates that inertial forces play a more dominant role. This is the Darcia body force compoent. $Da = \frac{K}{2L^2}$ an Darcian body forces disappear in a porous medium with infinite permeability when Da approaches infinite. Figure 8(a) demonstrates unambiguously that (f') is amplified with an increase in *Da*, with the maximum effect occurring close to the surface. Greater permeability, of course, indicates a decrease in solid Fibers that obstruct fluid flow, which accelerates the flow by lowering the Darcian resistance; this lowers the Darcian resistance and accelerates flow. As the Darcy parameter increases, the maximum velocity is pushed further from the wall. Yet again, increased permeability facilitates the magnetic polymer's percolation via the porous media. Figure 8(b) shows that boosting the Darcy parameter yields a significant suppression of (θ). Heat conduction is suppressed as a result of the loss of porous matrix containing solid fibres linked to increased penetration. This cools the regime by reducing heat diffusion inside it. As a result, the surface's heat BLT is suppressed. Porous media with lower permeability reach far higher (θ) than those with higher permeability. Figure 8(c) eluciates that as the *Da* increases this indicates increased resistance to flow through the porous medium. This resistance reduces the exchange of nanocrystals, leads to a low concentration of NPs near surface. Consequently, overall (ϕ) profile within the fluid decreases. *Our outcomes are consistent with the patterns of* [34, 35, 37]. Physically, Fluid flow resistance falls as *Da* rises, showing increased permeability in the porous medium. This lower resistance allows for an increased (f') because the flow encounters less drag. However, the enhanced (f') reduces leads to decay in both (θ) and (ϕ) profiles. Essentially, fluid moves more quickly through the medium, carrying less heat and fewer NPs along with it. Reduced heat transmission via thermal conduction in the system is facilitated by the steady reduction of solid fibres that have large *Da* values in porous medium. This cools down the thermal BLT, which also diminishes, and limits the transfer of energy from heat into the system from a vertical plane. As a result, the flow quickens, its (f') rises, and the momentum of the regime does too. This parameter is crucial for analysing and modelling fluid flow behaviours in applications using porous medium, including increased extraction of oil, flow of groundwater, and purification.

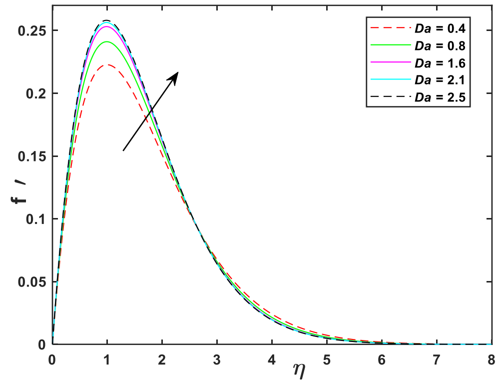

(a) Influence of Da on velocity profile

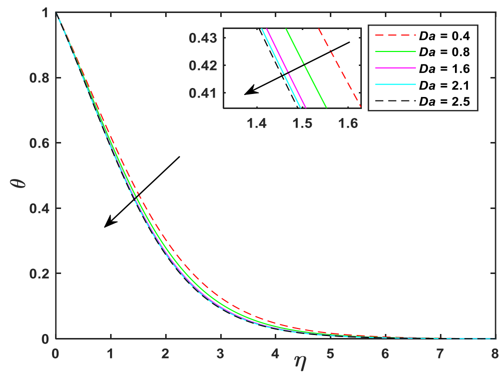

(b) Influence of Da on temperature profile

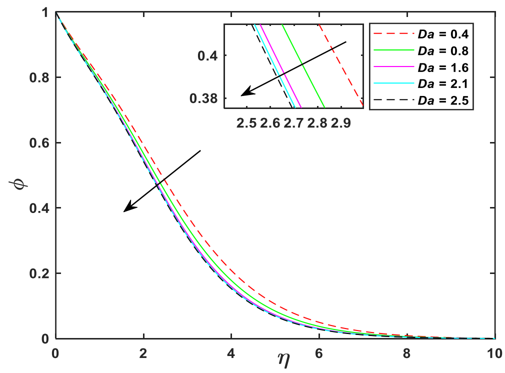

(c) Influence of Da on concentration profile

Figure 8. Effect of darcy parameter *Da* on velocity, temperature and concentration profiles

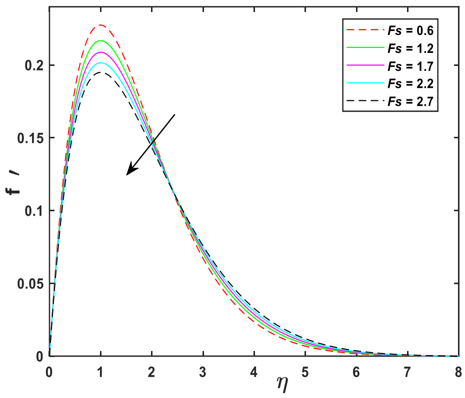

(a) Influence of *Fs* on velocity profile

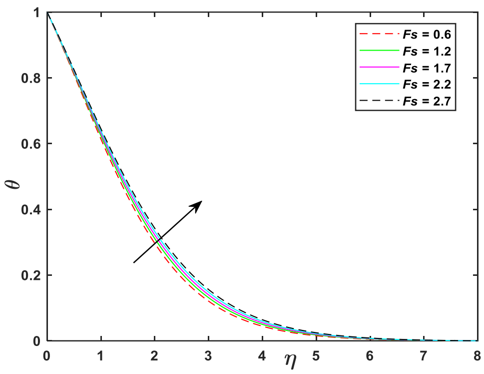

(b) Influence of Fs on temperature profile

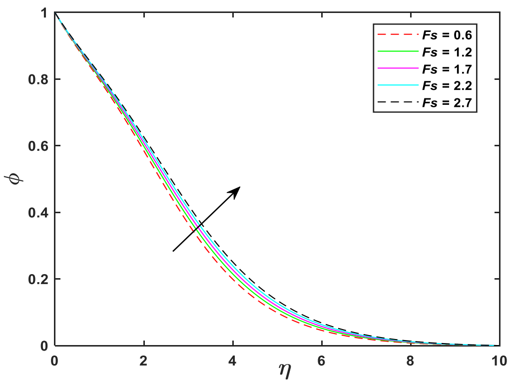

(c) Influence of Fs on Concentration Profile

Figure 9. Effect of Forchheimer parameter *Fs* on velocity, temperature and concentration profiles

Figures 9(a)-9(c) highlight the influence of the Forchheimer number (0≤*Fs*≤2.7) on ($f^{'}$), (*θ*), (*ϕ*). $Fs = \frac{2b}{L}$. (*Fs*) a non-dimensional parameter. It measures relative significance of viscous forces and inertial effects in a media with pores. This term $-\frac{Fs}{Da}\xi^2 f'^2$ appears in momentum Eq. (15), it compares inertial forces (which drive the flow) to viscous forces (which resist the flow). An increased value of (*Fs*) suggests that inertial forces gain greater prominence in comparison to viscous forces, thereby affecting the flow dynamics within the porous medium. (*Fs*) mimics the effects of second-order, nonlinear drag in porous material. In contrast to the linear Darcian drag components, it is quadratic, just like the Darcy number. In the case of Darcy-Brinkman flow, inertial drag effects disappear at Fs=0. Figure 9(a) demonstrates how a greater inertial impedance that resists flow is present and causes a noticeable depreciation in (f') with an increase in *(Fs)*. This impact is maximised close to surface, lesser deceleration in a flow with a higher *(Fs)* is calculated farther away. There is no discernible effect of *(Fs)* on flow in the free stream. Figure 9(b) reveals a significant heating impact occurs in the regime as a result of the higher (*Fs*). (*θ*) is always stronger for all transverse coordinate (η) values. Hence, thickness of the thermal BL is highest for the strong Forchheimer case (*Fs*=1) and smallest for weak Forchheimer drag case (*Fs*=0). Simulations performed by us are restricted to non-tortuous and isotropic porous medium. Nonetheless, second order inertial porous drag and linear Darcian impedance have a major impact on controlling flow and thermal properties in coating manufacturing processes. Figure 9(c) illustrates (*ϕ*) increases as (*Fs*) gradually rises because greater (*Fs*) signify greater inertial effects in flow through porous medium. These inertial effects enhance the mixing and dispersion of nanocrystals, leads to a greater (*ϕ*) of NPs near surface. Consequently, increased inertial forces facilitate better nanoparticle distribution and an elevated concentration profile. *Our observations correspond with the patterns of* [34, 35, 37]. Physically, since the drag force and coefficient of inertia are connected, a surge in inertia causes the fluid's drag force to grow, thus lowering its speed. The influence of the quadratic inertial drag is larger with closer proximity to the wall's surface. Nevertheless, since forchimmer drag is of order two, a rise in *Fs* virtually blanks the momentum development and causes a slowdown. Consequently, the reduced (f') decreases convective heat transfer rate, tends to higher temperatures near the surface. Simultaneously, the enhanced inertial effects promote better mixing and dispersion of NPs, increasing their concentration near surface. Thus, ($f^{'}$), dampens while (*θ*), (*ϕ*) profiles enhance with higher (*Fs*). (*Fs*) is used to optimize flow and performance in NF -based filtration systems and heat exchangers by accounting for inertial effects in porous media.

Figures 10(a)-10(c) displays implications of magnetic parameter (0.1≤*M*≤2.2), on ($f^{'}$), (*θ*), (*ϕ*) profiles through surface regime. Magnetic parameter $M = \frac{\sigma B_0^2 L^{\frac{1}{2}}}{\mu C_1^2}$ is also called as rotational Stuart number correlates centrifugal inertial force with Lorentzian magnetic drag force. It features in the term, $-M\xi f^{'}$ in momentum Eq. (15). Electrical non-conductivity of NF occurs when *M*=0 and magnetic field effects disappear. Because of varying (f') fields, magnetic force has a more complex effect. Figure 10(a) indicates that ($f^{'}$) appreciates as *M* value elevates, as the magnetic parameter increases, the Lorentz force (which opposes the flow) becomes stronger. However, in this scenario, the increased magnetic field may cause a damping effect on the fluid, reducing resistive forces from the porous medium. This results in a higher fluid (f') near the boundary, *which was not observed in the previous literature related to this kind of trend in magnetic interaction parameters*. Physically, the applied magnetic field modifies the flow dynamics, enhancing the momentum transfer in the NF. Figures 10(b)-10(c) show how raising the magnetic parameter depreciates both (*θ*), (*ϕ*) profiles as the magnetic parameter increases, the enhanced Lorentz force induces a stronger flow, which improves convective heat and mass transfer. This results in faster heat and mass removal from the BL region, leading to a decrease in both (*θ*), (*ϕ*). Physically, the magnetic field accelerates the fluid, reducing thermal and solutal BLT.

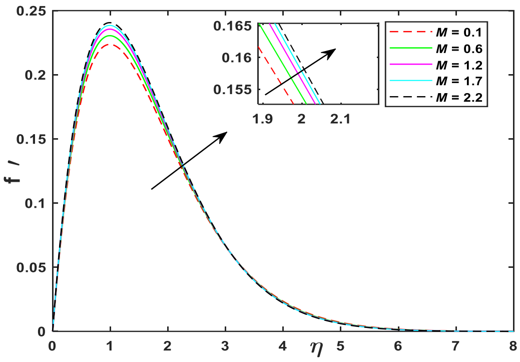

(a) Influence of M on Velocity Profile

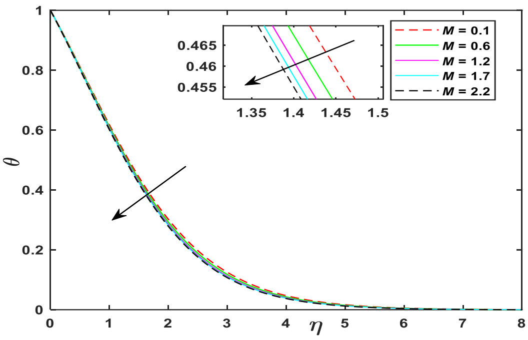

(b) Influence of M on temperature profile

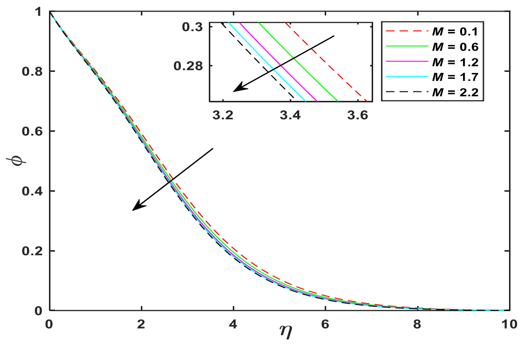

(c) Influence of M on concentration profile

Figure 10. Effect of magnetic parameter *M* on velocity, temperature and concentration profiles

Figures 11(a)-11(c) show how Eckert number ($0 \leq Ec \leq 4.5$), on (f'), (θ), (ϕ) profiles through surface regime with transverse coordinate (η). The dimensionless Eckert number $Ec = \frac{16\nu^2 C_1^4 L}{C_p(T_W - T_\infty)}$ is used to measure the effect of viscous dissipation in a flow. This term $Ec\xi^2 f''^2 + M(Ec)\xi^3 f'^2$ appears in the Eq. (16). *Ec* models the relative contribution of internal friction-induced kinetic energy dissipation to the BL enthalpy differential. It is produced by internal friction caused by molecule ballistic collisions in the magnetic polymer, which results in a heating effect. *Ec* also plays a part in the Ohmic heating term, commonly referred to as Joule heating, which characterizes the magnetic polymer's resistance to electrical current. Both viscous and Ohmic dissipation disappear when *Ec*=0. High values of *(Ec)* indicate that kinetic energy is significantly converted into internal energy through viscous friction, leading to noticeable temperature changes within the fluid. Figure 11(a) illustrates that (f') elevates when *Ec rises*. Higher *Ec* signifies greater kinetic energy relative to thermal energy, which promotes fluid motion due to viscous dissipation. (θ) rises because of this transformation of kinetic energy into thermal energy reducing viscosity, consequently increasing velocity. Figure 11(b) shows that as *Ec* enhances (θ) also appreciates significantly, viscous dissipation causes a larger conversion of kinetic energy into thermal energy. This mechanism, combined with extra heat via Ohmic heating and internal heat generation, raises the fluid's temperature. Figure 11(c) depicts that the *(ϕ)* declines as the *Ec* improves due to greater thermal energy from viscous dissipation and Ohmic heating which enhances Brownian motion of NPs. *Our observations correspond with the patterns of* [25, 34, 36]. Physically, the increased thermal agitation causes NPs to disperse farther away from the substrate, reducing their concentration. Additionally, elevated (θ) reduces fluid's capacity to carry on higher nanoparticle concentrations near the BL. This elevated (θ) enhances thermal diffusion, thereby reducing the concentration gradient and causing the concentration profile to decline. This underscores the inverse relationship between viscous heating and solute concentration in fluid flows.

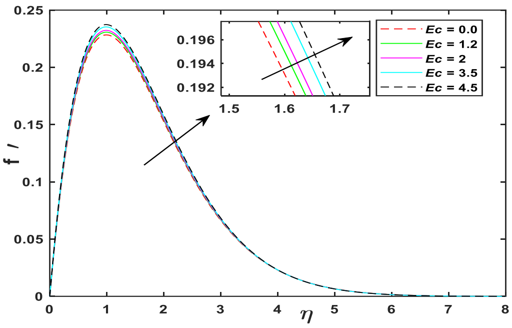

(a) Influence of Ec on velocity profile

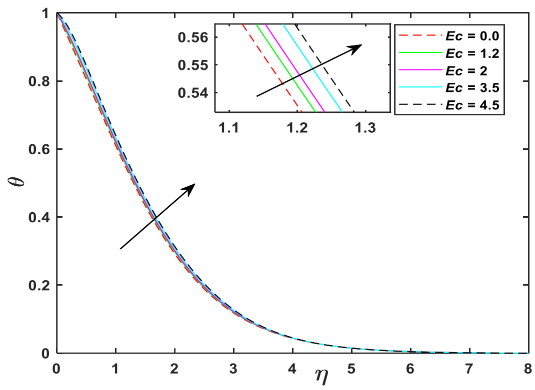

(b) Influence of Ec on temperature profile

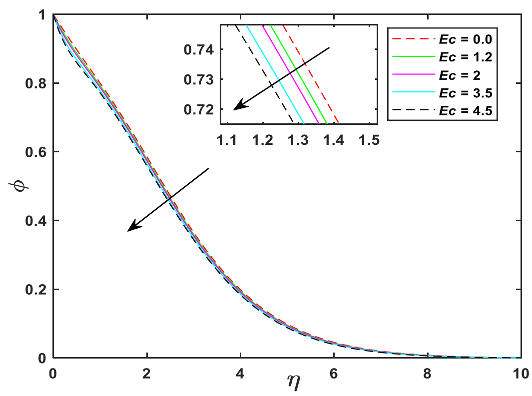

(c) Influence of Ec on concentration profile

Figure 11. Effect of Eckert number *Ec* on velocity, temperature and concentration profiles

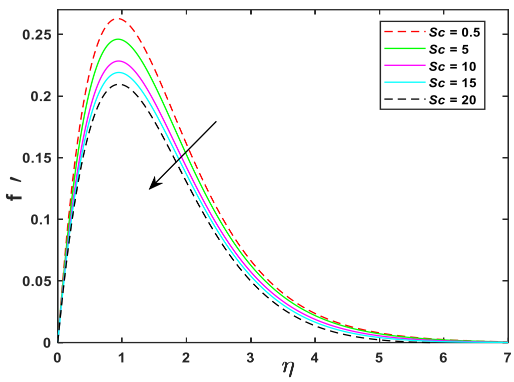

(a) Influence of Sc on velocity profile

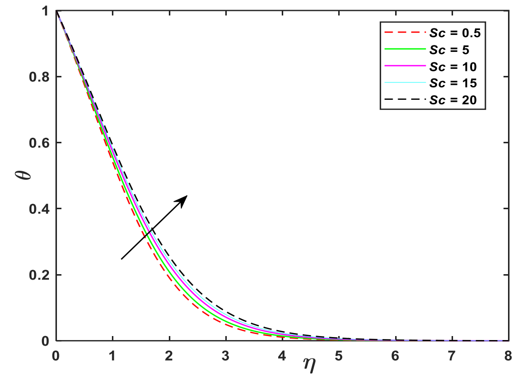

(b) Influence of Sc on temperature profile

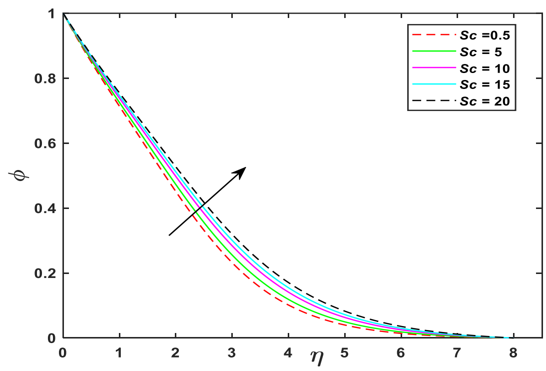

(c) Influence of Sc on concentration profile

Figure 12. Effect of schmidt number *Sc* on velocity, temperature and concentration profiles

Figures 12(a)-12(c) feature impact of Schmidt number ($0.5 \leq Sc \leq 20$) on profiles ($f^{'}$), (θ), (ϕ) through surface regime with transverse coordinate (η). Schmidt number (Sc) dimensionless number in that characterizes relative significance of mass diffusion (molecular diffusion) over momentum diffusion (viscous effects) in a fluid. Definition of it is mass diffusivity divided by kinematic viscosity, given as $Sc = \frac{\nu}{D_m}$, this term $\frac{\phi^{''}}{Sc}$ appears in concentration Eq. (17). (Sc) helps assess how momentum is transported relative to mass within the fluid, influencing the behaviours and distribution of NPs in various applications. Figure 12(a) depicts that ($f^{'}$) dampens with an increasing Schmidt number because a higher Schmidt number indicates lower mass diffusivity relative to momentum diffusivity. This results in a thicker solutal BL, which decreases fluid flow resistance and overall velocity. Consequently, fluid movement is slowed down, leading to a decreased velocity profile. Figures 12(b)-12(c) elucidates that (θ) and (ϕ) profiles substantially elevate with an enhanced (Sc) because a higher Schmidt number indicates lower mass diffusivity, leading to a thicker concentration BL. This results in less diffusion of NPs away from the surface, thereby increasing their concentration near the wall. Additionally, the thicker BL retains more heat, elevating (θ) profile. For $Sc<1$, species diffusivity dominates and vice versa for $Sc>1$, whereas a slight increase is observed in (θ) with increasing Sc, and a strong reduction in (ϕ) is seen with increasing Sc values. Our results are consistent with the trends observed by Gaffar et al. [42]. The practical use of (Sc) lies in enhancing mass transfer processes in areas like chemical reactors and separation systems by choosing NFs with suitable momentum and mass diffusion characteristics.

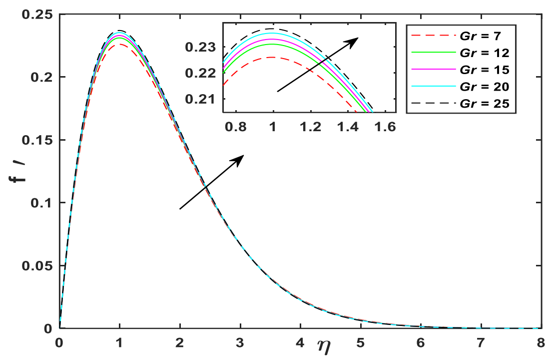

(a) Influence of Gr on velocity profile

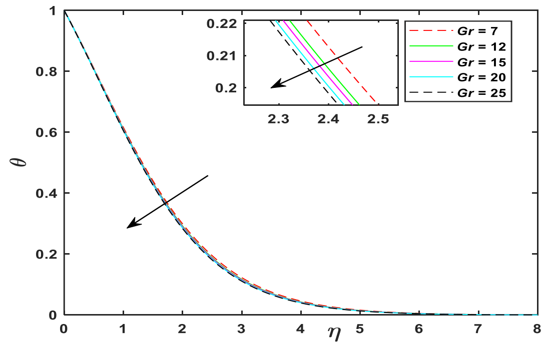

(b) Influence of Gr on temperature profile

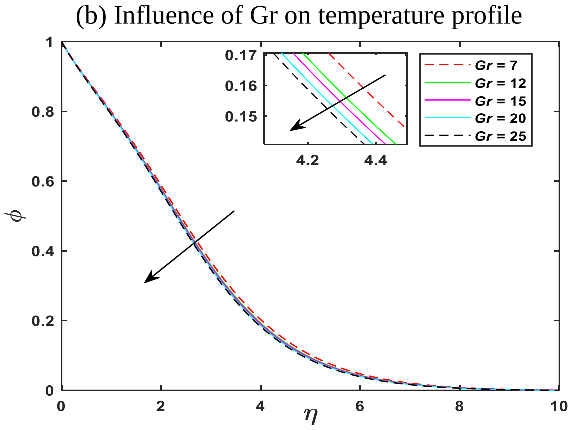

(c) Influence of *Gr* on concentration profile

Figure 13. Effect of Grashof number *Gr* on velocity, temperature and concentration profiles

Figures 13(a)-13(c) demonstrate the impact of Grashof number ($7 \leq Gr \leq 25$) on profiles ($f^{'}$), (θ), (ϕ) through surface regime with transverse coordinate (η). Grashof number (Gr) dimensionless number which quantifies the proportionate importance of buoyant and viscous forces in a fluid flow. It helps in understanding and optimizing heat transfer processes driven by buoyancy effects. The velocity profile is enhanced while (θ), (ϕ) profiles decrease. In Figures 13(a)-13(c) as the Grashof number (Gr) increases, (f') increases due to stronger buoyancy forces driving the flow, enhancing fluid motion. (θ), (ϕ) decrease because the intensified convection transfers heat and NPs more rapidly away from the surface, thinning the BLs. Physically, the (Gr) represents the ratio of buoyancy forces to viscous forces in the fluid. Higher (Gr) values indicate stronger buoyancy forces, which accelerate the fluid flow, thereby increasing the velocity profile. This enhanced flow promotes greater mixing and heat transfer, reducing (θ), (ϕ) gradients near the semi-infinite vertical plate. (Gr) in fluid dynamics, NFs are used to design and optimize systems where natural convection plays a critical role, such as in solar collectors, electronic cooling systems, and heating applications. It helps predict how buoyancy-driven flow affects heat and mass transfer, allowing for improved efficiency in these thermal management systems.

Figures 14(a)–14(c) demonstrate impacts of Eckert number Ec on (C_f), Nu, Sh along the surface regime. (C_f) increases indicating higher viscous dissipation, more kinetic energy is converted to thermal energy, which enhances (f') gradients, thereby rising (C_f). The increased (θ) gradients also intensify mass transfer, raising (Sh). However, added thermal energy reduces the temperature difference between fluid surfaces decreasing Nu, which measures heat transfer efficiency. Physically, this conversion increases (f') near the surface, thereby raising skin friction, higher thermal energy also enhances nanoparticle diffusion, leading to more effective mass transfer and thus boosting Sh. However, elevated internal thermal energy reduces the temperature gradient between fluid, and surface which is the driving force for convective heat transport, resulting in a lower Nusselt number. Thus, while momentum mass transfer is enhanced, the efficiency of heat transmission diminishes due to the reduced temperature differential. In electronic cooling systems, such as those in high-performance computers, increased viscous dissipation from rapidly moving coolant fluids generates heat, enhancing fluid velocity and mass transfer rates, analogous to higher (C_f), Sh.

It is noteworthy that in Figures 5-14 all profiles converge Seamlessly confirming the application of an appropriately large infinity boundary condition in the far-field region.

Table 3 shows the (C_f), (sh), (Nu) for various values of M, Pr, Sc, Da, and Fs along with a variation in the stream-wise coordinate value ξ,$(1 \leq \xi \leq 3)$. The following default parameter values are used: $Nr=0.1$, $Nb=0.3$, $Nt=0.3$, $Ec=0.5$, $Gr=10$.

It is observed that as the magnetic parameter (M) increases, the Lorentz force induced by the magnetic field enhances the fluid movement reducing (C_f), (Nu) which measures rate of heat transfer. This opposition leads to a thicker thermal BL. Conversely, enhanced M, raises mass transfer rate, leading to a higher Sh as concentration BL becomes thinner. *As Prandtl number Pr appreciates* the fluid's thermal diffusivity decreases, leading to a thicker thermal BL reducing (Nu). Elevation in Pr also means higher momentum diffusivity, which depreciates (C_f). Conversely, mass diffusivity is less affected, resulting in a thinner concentration BL and an increased Sh, indicating enhanced mass transfer. *As (Sc)* boosts it leads to a thinner concentration BL. This results in higher mass transfer rates, thus steadily rising (Sh). The reduced mass diffusivity also means higher momentum diffusivity, which increases velocity gradient at the wall, thereby raising (C_f). Furthermore, the enhanced flow mixing due to higher (Sc) contributes to surged heat transfer, resulting in a higher (Nu). As the (Da) number increases, the permeability of the porous medium rises, reducing resistance to fluid flow. This leads to higher fluid velocities near the wall, which elevates (C_f). The enhanced fluid motion improves both heat and mass transfer rates, resulting in higher (Nu), (Sh) due to thinner thermal and concentration BL. As *(Fs) rises significantly*, the inertial resistance in porous media becomes more significant. This increased resistance reduces (f), leading to a decrease in (C_f). Additionally, the lower (f') diminishes both thermal and mass transmission rates, resulting in reduced (Nu), (Sh) due to thicker thermal and concentration BL.

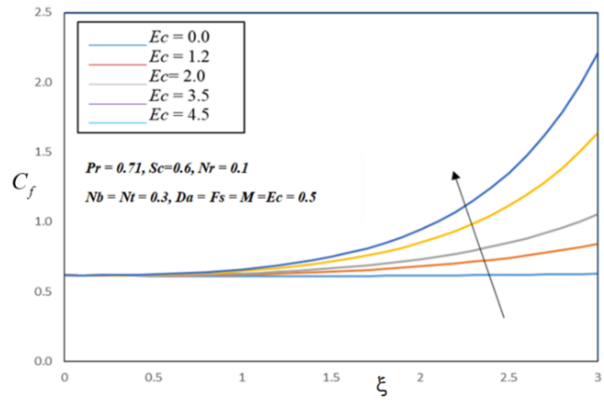

(a) Influence of Ec on skin friction

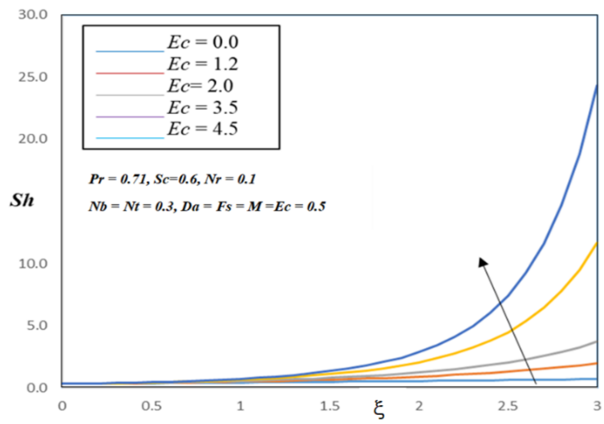

(b) Influence of Ec on sherwood number

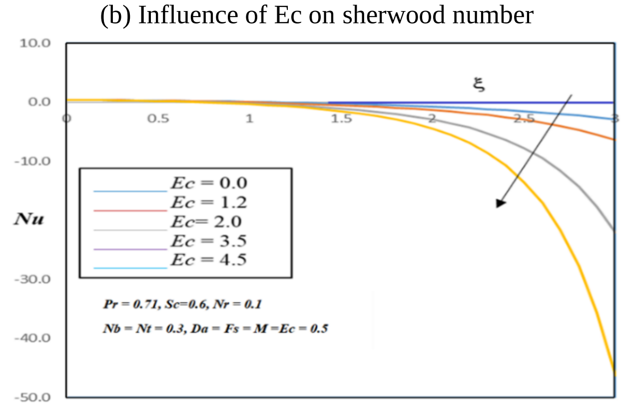

(c) Influence of Ec on Nusselt number

Figure 14. Effect of Eckert number Ec on (C_f), (Nu), (Sh)

Table 3. Values of skin friction (C_f), Sherwood number (Sh), and Nusselt number (Nu) for various values of *M, Pr, Sc, Da, and Fs*

					x=1			x=2			x=3		
M	***Pr***	***Sc***	***Da***	***Fs***	C_f	***Sh***	***Nu***	C_f	***Sh***	***Nu***	C_f	***Sh***	***Nu***
0.1					0.6538	0.4595	0.1663	0.7044	0.6913	-0.2435	0.7789	1.0699	-0.9435
0.6					0.6058	0.4421	0.1338	0.6253	0.6757	-0.3335	0.6888	1.0968	-1.2020
1.2					0.5576	0.4255	0.0969	0.5551	0.6725	-0.4377	0.6138	1.1604	-1.5138
1.7					0.5240	0.4152	0.0680	0.5107	0.6787	-0.5212	0.5688	1.2293	-1.7776
2.2					0.4953	0.4077	0.0404	0.4752	0.6900	-0.6021	0.5342	1.3086	-2.0478
	0.71				0.8859	0.6184	0.3013	1.0847	0.6015	0.2465	0.2249	0.5615	0.1211
	7				0.8436	0.6178	0.3200	1.0331	0.6030	0.2615	0.2062	0.5645	0.1265
	10				0.7667	0.6266	0.3365	0.9404	0.6151	0.2737	0.1753	0.5750	0.1283
	15				0.7306	0.6417	0.3257	0.8976	0.6305	0.2633	0.1622	0.5848	0.1206
	25				0.6980	0.6750	0.2830	0.8599	0.6614	0.2257	0.1510	0.6012	0.0988
		0.5			0.4953	0.4077	0.0404	0.4752	0.6900	-0.6021	0.5342	1.3086	-2.0478
		5			0.6389	1.2280	0.1047	0.6542	1.3713	-0.3097	0.7092	1.6445	-1.0732
		10			0.6413	1.5821	0.1034	0.6549	1.7005	-0.2934	0.7075	1.9364	-1.0249
		15			0.6422	1.8255	0.1040	0.6550	1.9312	-0.2827	0.7067	2.1495	-0.9963
		20			0.6426	2.0178	0.1049	0.6551	2.1154	-0.2750	0.7064	2.3232	-0.9764
			0.4		0.5144	0.1465	0.3971	0.4429	0.1196	0.3489	0.3900	0.1043	0.3090
			0.8		0.5536	0.1631	0.4206	0.5040	0.1431	0.3900	0.4591	0.1267	0.3596
			1.6		0.5730	0.1713	0.4317	0.5399	0.1634	0.4120	0.5109	0.3906	0.3835
			2.1		0.5822	0.1751	0.4368	0.5587	0.1800	0.4227	0.5344	0.1290	0.4077
			2.5		0.5846	0.1761	0.4381	0.5658	0.2317	0.4252	0.5421	0.1832	0.4111
				0.6	0.5268	0.1519	0.4046	0.4592	0.1258	0.3600	0.4067	0.1090	0.3213
				1.2	0.5136	0.1473	0.3958	0.4339	0.1179	0.3406	0.3773	0.1027	0.2967
				1.7	0.5037	0.1438	0.3891	0.4176	0.1133	0.3277	0.3600	0.1000	0.2821
				2.2	0.4947	0.1406	0.3829	0.4043	0.1099	0.3170	0.3465	0.0985	0.2705
				2.7	0.4865	0.1377	0.3771	0.3931	0.1072	0.3078	0.3355	0.0975	0.2611

5. CONCLUSIONS

A mathematical model of steady-state laminar coating BL flow of magnetized Buongiorno nanofluid from a semi-infinite vertical surface to a non-darcy porous media has been developed. MHD and viscous dissipation effects, Thermal convection and nanoparticle mass transport have also been incorporated. The governing equations and BCs have been made dimensionless through suitable scaling and non-similar transformations. The subsequent nonlinear multi-physical BVP was then solved with a second-order implicit finite-difference KBM, implemented in MATLAB. The Keller box code has been validated with previously published research. Graphical and tabulated Results about how several factors affect transport characteristics have been shown.

Computations have shown that:

(i) With an elevation in *Nb*, (f') and (θ) profiles are amplified on the contrary, the (ϕ) profile is suppressed throughout the BL regime.

(ii) An increase in thermophoresis parameter (*Nt)* fluid the flow is significantly slowed down farther away from the surface, however, strongly enhances thermal and nanoparticle species BLT, which can have a significant influence on the homogeneity of nano-coatings in the manufacturing process.

(iii) A heightened buoyancy ratio parameter (*Nr*) strengthens buoyancy-driven flows, declines fluid motion, and enhances (θ), (ϕ) significantly.

(iv) Strong fluid flow acceleration is produced close to the plate's surface by an increase in the Darcy parameter (*Da*) because of increased permeability, yet (θ), (ϕ) of NPs are significantly suppressed across BL that is transverse to the substrate.

(v) Higher (*Fs*) reduces (f') due to increased inertial resistance, but (θ), (ϕ) surge throughout the BL transverse to the wall as reduced convective heat transfer allows more heat and better nanoparticle distribution.

(vi) An enhancement in magnetic interaction parameter *M*, accelerates fluid flow, in the vicinity of the plate's surface, but significantly depletes (θ), (ϕ), because of the heat generated during the process of pulling the magnetic polymer against the radial magnetic field.

(vii) Considerable rise of Eckert number (*Ec*) boosts (f') by transforming kinetic energy into thermal energy and reducing viscosity. Higher (*Ec*) also accelerates (θ) while decreasing (ϕ), as viscous dissipation promotes greater thermal energy and dispersion.

(viii) Higher Prandtl number (*Pr*) decreases thermal diffusivity, resulting in a thicker thermal BL and reduced (*Nu*), (C_f).

(ix) As Schmidt number (*Sc*) increases it enhances (C_f), mass transfer rate (*Sh*), heat transfer rate (*Nu*).

(x) An increase in (*Da*) raises fluid permeability (f') and in turn enhancing (C_f), mass transfer rate (*Sh*), heat transfer rate (*Nu*). On the other hand, a higher (*Fs*) increases inertial resistance, reducing (C_f), mass transfer rate (*Sh*), heat transfer rate (*Nu*).

The present study has revealed some interesting characteristics of semi-infinite substrate magnetic NF coating BL flows. This has practical implications for enhancing design and optimization of cooling systems, enhancing thermal properties of coatings electronic thermal management, and energy systems, where precise thermal control and efficient heat transfer are critical. This study fills the gap by incorporating all these aspects into a comprehensive mathematical model, offering new insights into the complex interplay between magnetic fields, heat and mass transfer, and NF behavior in porous structures that deviate from Darcy's law. "Keller's box method is very efficient in solving this complex multi-physical coating BVP. The study provides a foundation for designing efficient thermal management systems by utilizing magneto-dissipative NFs to enhance heat transfer in porous structures. Its findings can be applied to optimize cooling in electronic devices, heat exchangers, and microfluidic systems where localized thermal control is essential. The ability to manipulate thermal conductivity via external magnetic fields enables adaptive and energy-efficient cooling solutions. Furthermore, the study's insights into controlled heat and mass transfer in magneto-dissipative NF flows can be directly applied to optimize coating uniformity and thickness in thermal spray and dip-coating processes. By tuning magnetic fields and nanoparticle pattern, enhanced adhesion and thermal stability of coatings on porous substrates can be achieved. This is particularly beneficial in industries requiring high-performance coatings, such as aerospace, biomedical, and microelectronics.

As a result, future research may examine non-Newtonian polymeric models, such as viscoelastic and shear-thinning formulations, which will be presented shortly.

REFERENCES

[1] Sus, C. (1995). Enhancing thermal conductivity of fluids with nanoparticles, developments and applications of non-Newtonian flows. Siginer DA, Wang HP (Eds.). FED-The American Society of Mechanical Engineers. ASME, FED, MD, 231: 99-I05.

[2] Eastman, J.A., Phillpot, S.R., Choi, S.U.S., Keblinski, P. (2004). Thermal transport in nanofluids. A Annual Review of Materials Research, 34(1): 219-246. https://doi.org/10.1146/annurev.matsci.34.052803.090621

[3] Buongiorno, J. (2006). Convective Transport in Nanofluids. ASME Journal of Heat and Mass Transfer, 128(3): 240-250. https://doi.org/10.1115/1.2150834

[4] Ahmad, L., Ahmed, J., Ahmed, A. (2022). Thermal energy transport in thin film flow of nanofluid over a decelerating rotating disk. Proceedings of The Institution of Mechanical Engineers, Part E: Journal of Process Mechanical Engineering, 236(2): 491-499. https://doi.org/10.1177/09544089211050717

[5] Khan, M., Sarfraz, M., Ahmed, J., Ahmad, L., Fetecau, C. (2020). Non-Axisymmetric Homann stagnation-Point flow of Walter’s B nanofluid over a cylindrical disk. Applied Mathematics and Mechanics, 41(5): 725-740. https://doi.org/10.1007/s10483-020-2611-5

[6] Ahmad, L., Ahmed, J., Khan, M., Yasir, M., Alghamdi, M. (2021). Effectiveness of Cattaneo-Christov double diffusion in Sisko fluid flow with variable properties: Dual solutions. Journal of Thermal Analysis and Calorimetry, 143: 3643-3654. https://doi.org/10.1007/s10973-019-09223-3

[7] Uddin, M.J., Hasan, M.M., Faroughi, S.A. (2024). Convective transport in a nanofluid-Filled annulus with an eccentric hypocycloid within a square disk. International Journal of Thermofluids, 22: 100664. https://doi.org/10.1016/j.ijft.2024.100664

[8] Humane, P.P., Patil, V.S., Patil, A.B., Shamshuddin, M.D. (2023). Buongiorno modelled nanoliquid consequence of thermal and solutal convection on the Magneto-Micropolar fluid inside an inclined porous stretching device. Journal of Nanofluids, 12(1): 211-222. https://doi.org/10.1166/jon.2023.1949

[9] Darcy, H. (1856). Les fontaines publiques de la ville de Dijon: Exposition et application des principes à suivre et des formules à employer dans les questions de distribution d'eau. Victor Dalmont, Vol. 1.

[10] Forchheimer, P.H. (1901). Wasserbewegung durch boden: Zeitschrift des Vereines Deutscher Ingenieure, 45: 1782-1788.

[11] Muskat, M. (2023). The flow of homogeneous fluids through porous media (Edwards, 1946). Scientific Reports, 13: 2666.

[12] Pal, D., Mondal, H. (2012). Hydromagnetic convective diffusion of species in Darcy-Forchheimer porous medium with non-Uniform heat source/sink and variable viscosity. International Communications in Heat and Mass Transfer, 39(7): 913-917. https://doi.org/10.1016/j.icheatmasstransfer.2012.05.012

[13] Yuan, W., Laima, S., Gao, D., Chen, W.L., Li, H. (2021). Influence of porous media coatings on flow characteristics and vortex-Induced vibration of circular cylinders. Journal of Fluids and Structures, 106: 103365. https://doi.org/10.1016/j.jfluidstructs.2021.103365

[14] Venkatadri, K., Öztop, H.F., Prasad, V.R., Parthiban, S., Bég, A.O. (2024). RSM-Based sensitivity analysis of hybrid nanofluid in an enclosure filled with non-Darcy porous medium by using LBM method. Numerical Heat Transfer, Part A: Applications, 85(6): 875-899. https://doi.org/10.1080/10407782.2023.2193708

[15] Ferdows, M., Alshuraiaan, B., Nima, N.I. (2022). Effects of non-Darcy mixed convection over a horizontal cone with different convective boundary conditions incorporating gyrotactic microorganisms on dispersion. Scientific Reports, 12(1): 16581. https://doi.org/10.1038/s41598-022-18549-2

[16] Umavathi, J.C., Bég, O.A. (2022). Computation of Von Karman thermo-solutal swirling flow of a nanofluid over a rotating disk to a non-Darcian porous medium with hydrodynamic/thermal slip. Journal of Thermal Analysis and Calorimetry, 147(15): 8445-8460. https://doi.org/10.1007/s10973-021-11126-1

[17] Wang, F., Saeed, A.M., Puneeth, V., Shah, N.A., Anwar, M.S., Geudri, K., Eldin, S.M. (2023). Heat and mass transfer of Ag-H2O nano-Thin film flowing over a porous medium: A modified Buongiorno’s model. Chinese Journal of Physics, 84: 330-342. https://doi.org/10.1016/j.cjph.2023.01.001

[18] Nasir, M., Waqas, M., Bég, O.A., Znaidia, S., Khan, W.A., Zamri, N. (2023). Functional magnetic Maxwell viscoelastic nanofluids for tribological coatings-A model for stretching flow using the generalized theory of heat-Mass fluxes, Darcy-Forchheimer formulation and dual convection. Tribology International, 187: 108610. https://doi.org/10.1016/j.triboint.2023.108610

[19] Saini, G., Hanumagowda, B.N., Mulki, H., Raju, S.S.K., Varma, S.V.K., Barghout, K., Murshid, N., Al-Kouz, W. (2023). Entropy generation optimization in couple stress fluid flow with variable viscosity and aligned magnetic field. Sustainability, 15(3): 2493. https://doi.org/10.3390/su15032493

[20] Novikau, I.S., Zverev, V.S., Novak, E.V., Kantorovich, S.S. (2023). Stockmayer supracolloidal magnetic polymers under the influence of an applied magnetic field and a shear flow. Journal of Molecular Liquids, 384: 122229. https://doi.org/10.1016/j.molliq.2023.122229

[21] Bi, Z., Gao, F., Liu, M., Zhang, R., Liu, R., Cui, G., Xu,

J. (2022). Multifunctional self-healing coatings with orderly distributed microcapsules aligned by magnetic field. Chemical Engineering Journal, 450: 138250. https://doi.org/10.1016/j.cej.2022.138250

[22] Moreira, J., Vale, A.C., Alves, N.M. (2021). Spin-Coated freestanding films for biomedical applications. Journal of Materials Chemistry B, 9(18): 3778-3799. http://dx.doi.org/10.1039/D1TB00233C

[23] Shoaib, M., Raja, M.A.Z., Sabir, M.T., Islam, S., Shah, Z., Kumam, P., Alrabaiah, H. (2020). Numerical investigation for rotating flow of MHD hybrid nanofluid with thermal radiation over a stretching sheet. Scientific Reports, 10(1): 18533. https://doi.org/10.1038/s41598-020-75254-8

[24] Ramana, R.M., Dharmaiah, G., Kumar, M.S., Fernandez-Gamiz, U., Noeiaghdam, S. (2024). Numerical performance of Hall current and Darcy-Forchheimer influences on dissipative Newtonian fluid flow over a thinner surface. Case Studies in Thermal Engineering, 60: 104687. https://doi.org/10.1016/j.csite.2024.104687

[25] Reddy, R., Gaffar, S.A. (2024). Chemical reaction and viscous dissipative effects on buongiorno's nanofluid model past an inclined plane: A numerical investigation. International Journal of Applied and Computational Mathematics, 10(2): 81. https://doi.org/10.1007/s40819-024-01723-7

[26] Shahzad, F., Jamshed, W., Nisar, K.S., Khashan, M.M., Abdel-Aty, A.H. (2021). Computational analysis of Ohmic and viscous dissipation effects on MHD heat transfer flow of Cu-PVA Jeffrey nanofluid through a stretchable surface. Case Studies in Thermal Engineering, 26: 101148. https://doi.org/10.1016/j.csite.2021.101148

[27] Awais, M., Awan, S.E., Raja, M.A.Z., Shoaib, M. (2021). Effects of gyro-Tactic organisms in bio-Convective nano-Material with heat immersion, stratification, and viscous dissipation. Arabian Journal for Science and Engineering, 46: 5907-5920. https://doi.org/10.1007/s13369-020-05070-9

[28] Sparrow, E.M., Quack, H., Boerner, C.J. (1970). Non-Similarity boundary-Layer solutions. American Institute of Aeronautics and Astronautics Jopurnal, 8(11): 1936-1942. https://doi.org/10.2514/3.6029

[29] Sparrow, E.M., Yu, H.S. (1971). Local non-Similarity thermal boundary-Layer solutions. ASME Journal of Heat and Mass Transfer, 93(4): 328-334. https://doi.org/10.1115/1.3449827

[30] Minkowycz, W.J., Sparrow, E.M. (1974). Local nonsimilar solutions for natural convection on a vertical cylinder. Journal of Heat Transfer, 96(2): 178-183. https://doi.org/10.1115/1.3450161

[31] Razzaq, R., Farooq, U. (2021). Non-similar forced convection analysis of Oldroyd-B fluid flow over an exponentially stretching surface. Advances in Mechanical Engineering, 13(7): 16878140211034604. https://doi.org/10.1177/16878140211034604

[32] Alsallami, S.A., Ahmad, L., Khan, I.U., Weera, W., Ullah, I., Yassen, M.F., El Bouz, M.A. (2023). Non-similar mathematical and dynamical analysis of Cross nano-Materials over a gravitationally effected surface. Ain Shams Engineering Journal, 14(8): 102035. https://doi.org/10.1016/j.asej.2022.102035

[33] Jan, A., Mushtaq, M., Hussain, M. (2024). Nonsimilar analysis of forced convection radially magnetized ternary hybrid nanofluid flow over a curved stretching surface. Numerical Heat Transfer, Part B: Fundamentals, 1-29. https://doi.org/10.1080/10407790.2024.2353790

[34] Ramesh Reddy, P., Abdul Gaffar, S., Anwar Beg, O., Md. Hidayathulla Khan, B. (2022). Hall and ion-slip effects on nanofluid transport from a vertical surface: Buongiorno's model. ZAMM-Journal of Applied Mathematics and Mechanics/Zeitschrift für Angewandte Mathematik und Mechanik, 102(3): e202000174. https://doi.org/10.1002/zamm.202000174

[35] Gaffar, S.A., Bég, O.A., Kuharat, S., Bég, T.A. (2024). Computation of hydromagnetic tangent hyperbolic non-Newtonian flow from a rotating non-Isothermal cone to a non-Darcy porous medium with thermal radiative flux. Physics Open, 19: 100216. https://doi.org/10.1016/j.physo.2024.100216

[36] Ramya, D., Raju, R.S., Rao, J.A., Chamkha, A.J. (2018). Effects of velocity and thermal wall slip on magnetohydrodynamics (MHD) boundary layer viscous flow and heat transfer of a nanofluid over a non-Linearly-Stretching sheet: A numerical study. Propulsion and Power Research, 7(2): 182-195. https://doi.org/10.1016/j.jppr.2018.04.003

[37] Anjum, A., Gaffar, S.A., Kumar, S., Peerusab, S. (2024). Dissipative magneto-thermo-convection of nanofluid past through a Semi-Infinite vertical surface with ohmic heating. Journal of Applied and Computational Mechanics, 1-18. https://doi.org/10.22055/jacm.2024.47689.4765

[38] Prasad, V.R., Gaffar, S.A., Reddy, E.K., Beg, O.A. (2014). Computational study of non-Newtonian thermal convection from a vertical porous plate in a non-Darcy porous medium with Biot number effects. Journal of Porous Media, 17(7): 601-622. https://doi.org/10.1615/JPorMedia.v17.i7.40

[39] Kuznetsov, A.V., Nield, D.A. (2010). Natural convective boundary-layer flow of a nanofluid past a vertical plate. International Journal of Thermal Sciences, 49(2): 243-247. https://doi.org/10.1016/j.ijthermalsci.2009.07.015

[40] Keller, H.B. (1978). Numerical methods in boundary-Layer theory. Annual Review of Fluid Mechanics, 10: 417-433. https://doi.org/10.1146/annurev.fl.10.010178.002221

[41] Bég, O.A., Prasad, V.R., Vasu, B., Reddy, N.B., Li, Q., Bhargava, R. (2011). Free convection heat and mass transfer from an isothermal sphere to a micropolar regime with Soret/Dufour effects. International Journal of Heat and Mass Transfer, 54(1-3): 9-18. https://doi.org/10.1016/j.ijheatmasstransfer.2010.10.005

[42] Gaffar, S.A., Prasad, V.R., Reddy, E.K. (2017). Computational study of Jeffrey's non-Newtonian fluid past a semi-infinite vertical plate with thermal radiation and heat generation/absorption. Ain Shams Engineering Journal, 8(2): 277-294. https://doi.org/10.1016/j.asej.2016.09.003

[43] Rafique, K., Anwar, M.I., Misiran, M., Khan, I., Seikh, A.H., Sherif, E.S.M., Nisar, K.S. (2019). Numerical analysis with Keller-Box scheme for stagnation point effect on flow of micropolar nanofluid over an inclined surface. Symmetry, 11(11): 1379. https://doi.org/10.3390/sym11111379

[44] Vajravelu, K., Prasad, K.V. (2014). Keller-Box method and its application. Walter de Gruyter GmbH & Co KG. Berlin, Boston: De Gruyter Studies in Mathematical Physics, De Gruter, USA, Vol. 8.

https://doi.org/10.1515/9783110271782

[45] Khan, B.M.H., Gaffar, S.A., Bég, O.A., Kadir, A., Reddy, P.R. (2020). Computation of Eyring-Powell micropolar convective boundary layer flow from an inverted non-Isothermal cone: Thermal polymer coating simulation. Computational Thermal Sciences: An International Journal, 12(4): 329-344. https://doi.org/10.1615/2020033860

[46] Ramachandra Prasad, V., Abdul Gaffar, S., Keshava Reddy, E., Anwar Bég, O., (2014). Flow and heat transfer of Jefferys non-Newtonian fluid from a horizontal circular cylinder. Journal of Thermophysics and Heat Transfer, 28(4): 764-770. https://doi.org/10.2514/1.T4253

[47] Bég, O.A. (2013). Numerical methods for multi-physical magnetohydrodynamics. Journal of Magnetohydrodynamics and Plasma Research, New Developments in Hydrodynamics Research, Nova Science, New York, 18(2/3): 93.

[48] Plumb, O.A., Huenefeld, J.C. (1981). Non-Darcy natural convection from heated surfaces in saturated porous media. International Journal of Heat and Mass Transfer, 24(4): 765-768. https://doi.org/10.1016/0017-9310(81)90020-X

[49] Chamkha, A.J., Rashad, A.M., RamReddy, C., Murthy, P.V.S.N. (2014). Viscous dissipation and magnetic field effects in a non-Darcy porous medium saturated with a nanofluid under convective boundary condition. Special Topics & Reviews in Porous Media: An International Journal, 5(1): 27-39. https://doi.org/10.1615/SpecialTopicsRevPorousMedia.v5.i1.30

[50] Merkin, J.H., Pop, I. (1996). Conjugate free convection on a vertical surface. International Journal of Heat and Mass Transfer, 39(7): 1527-1534. https://doi.org/10.1016/0017-9310(95)00238-3

[51] Siddiqa, S., Begum, N., Hossain, M.A., Abrar, M.N., Gorla, R.S.R., Al-Mdallal, Q. (2021). Effect of thermal radiation on conjugate natural convection flow of a micropolar fluid along a vertical surface. Computers & Mathematics with Applications, 83: 74-83. https://doi.org/10.1016/j.camwa.2020.01.011

NOMENCLATURE

B	magnetic field vector (Tesla), C_w
B_0	constant transverse (radial) magnetic field (Tesla), C_∞
b	inertial drag coefficient (-), V
Da	Darcy number (-), Nu
Fs	Forchheimer number (-), Sh
Ec	Eckert number (-), C_p
Pr	Prandtl number (-), M
Sc	Schmidt number (-), p
Gr	local Grashof number (-), C_f
x	streamwise coordinate (m)
y	transverse coordinate (m), θ
u	dimensionless velocity components in x direction (m/s), ϕ
v	dimensionless velocity components in y direction(m/s), μ
Nb	Brownian motion parameter (-), ν
Nt	thermophoresis parameter (-), ξ
Nr	Buoyancy ratio parameter (-), η
f	non-dimensional stream function, ψ
g	acceleration due to gravity (m/s^2), μ_f
L	characteristic length (m), ν_f
D_B	Brownian diffusion coefficient (m^2/s), ρ *(or)* ρ_f
Dm	molecular diffusivity (m^2/s), σ *(or)* σ_f
D_T	thermophoretic diffusion coefficient (m^2/s), ρ_p
K	permeability (-), α *(or)* α_m
k	thermal conductivity of the fluid (W/mK), β
k_m	effective thermal conductivity (W/mK), ρC_p
C	nanoparticle volume fraction (-), τ
T	temperature of the fluid (Kelvin)
T_w	wall temperature (K), w
T_∞	ambient temperature (K), ∞
D	nanoparticle diffusivity